University of Bremen

Alfred Wegener Institute, Helmholtz Centre for Polar and Marine Research

Master thesis

Analysis of the seasonality based on the angular calendar in paleo-climate simulations with AWI-ESM

Author:
Endurance Igbinosa

Matriculation Number:
3118960

First Supervisor:
Prof. Dr. Gerrit Lohmann

Second Supervisor:
Dr. Christoph Voelker

Tutor:
Dr. Xiaoxu Shi

October, 2021

Declaration of copyright

I hereby declare that my Master's Thesis was written without external support and that I did not use any other sources and auxiliary means than those quoted. All statements which are literally or analogously taken from other publications have been identified as quotations and citations.

Declaration with regard to publishing this thesis

I agree that for research purposes third parties can use my thesis stored in the University archive.

Bremen / October 2021 **Igbinosa Endurance.O.**

Abstract

Orbital forcing is a major driver of climate variability on timescales of 10,000 to 100,000 years. The orbital parameters responsible for these changes are Eccentricity, Obliquity and Procession. For comparison between simulated paleo and present climate, biases in seasonality may emerge without the use of the angular calendar, as in the today's classical calendar, the start/end of one season may correspond to different angles between the vernal equinox and the earth. On the other hand, model resolution is also an important factor for resolving some small-scale process in the simulated world. Hence, the Alfred Wegener Institute has established and developed the state-of-the-art high.-resolution Earth system models AWI-ESM1 and AWI-ESM2, with the ice-ocean component being based on finite element/volume formation.

In this study, we take advantage of the simulation results from AWI-ESM1 and AWI-ESM2. Climate variables such as surface temperature and precipitation are analyzed and compared between paleo and modern climate conditions. The simulations for mid-Holocene (MH, 6k B.P.) and Last Inter-glacial (LIG, 127k B.P.) were designed to examine the climate responses to changes in orbital forcings and greenhouse gases. The continental configuration remains unchanged with respect to the pre-industrial (PI) condition. Due to the insolation anomaly induced by orbital configuration, the seasonality for the MH is larger than today resulting from the positive anomaly of solar insolation in boreal summer and autumn, and negative anomalies during winter time. The Antarctic was colder in DJF and MAM and warmer in JJA and SON in the MH as compared to present. There was more precipitation in the MH over the tropical rain belt as a result of a northward shift of the inter-tropical convergence zone (ITCZ).

Additionally, there is an enhanced seasonality in the LIG as compared to present-day for the simulated surface temperature with a cooling of up to 5 K in boreal winter and warming of more than 5 K for boreal summer. Furthermore, a stronger summer monsoon over the Northern Hemisphere monsoon domains, including the North America, South Asia, and Western Africa, is observed in the LIG when compared to PI which is accompanied by a pronounced increase in precipitation, which mimics the pattern of the MH but much stronger in magnitude.

However, seasonality definition of paleo-climate based on present-day fixed calendar can lead to biases for the seasonal changes. In the present study, we

performed calendar correction onto the simulated PI, MH and LIG climate. The results show that, generally the classical calendar tends to underestimate the warming over MH/LIG northern hemisphere especially during SON. The temperature anomalies in MH/LIG SON with regards to PI can even flip its sign after calendar conversion. Moreover, the classical calendar overestimate and underestimate the MH and LIG Africa summer monsoon precipitation for JJA and SON respectively. Our study indicates the importance of seasonality definition on investigating the past climate.

In addition, we also explored the calendar effect on surface air temperature and precipitation in a transient simulation for the past 6000 years, in which we varied the greenhouse gases and orbital parameters while keep other boundary conditions unchanged. Our main focus was NH continents as they appear to have the most pronounced response to calendar conversion. Anomalies in NH temperatures (between angular and classical means) over land tend to have different trends in different seasons. For DJF and MAM, there is a gradual decline in the temperature differences from 6K to present associated with calendar correction. The temperature bias is not strong owing to the fact that, the beginning and end of summer in angular calendar for 0k is similar as in our fixed-length calendar used today. The mean angular-minus-classical temperature in SON present a pronounced warming from 6k to 3k, and an obvious cooling from 3k to 0k. The strong bias around 6k in SON results from the large shift in autumn days (6 days) between angular and classical calendars. Similar trend is noticed over the Northern Hemisphere ocean, though with a smaller magnitude. On the other hand, we found a noticeable calendar effect on precipitation, especially over the Africa Monsoon domain in summer and autumn months. Under present fixed-length calendar, the Africa monsoon rainfall is largely underestimated, and such bias becomes weaker from 6k to 0k.

Another topic of the present thesis is the characteristic of El Nino and ther Southern Oscillation (ENSO) in a transient study which was carried out using AWI-ESM2. In-order to investigate the evolution of ENSO we examined the Nino3.4 index, which is calculated as the sea surface temperature anomalies over the region 5N-5S, 170W-120W. In this new study, inter-annual variability and seasonality of the Nino3.4 index was investigated. In addition, composite analysis is performed to further investigate the climate response to ENSO through time (i.e 6k - 0k) regionally and globally. Our results indicate an increase in both inter-annual variability and seasonality of ENSO through

time. We also found a negative correlation between the Nino3.4 index and the precipitation over all Northern Hemisphere monsoon domains. Considering the rising trend in Nino3.4 index and its strengthened variability from 6k to 0k, we could conclude that extreme dry events in present-day very likely occur more often than in the mid-Holocene. Seasoanlity on the other hand has shown an increase which has peak around 2k before attaining steady increase. However, the changes in seasonality can result from ENSO magnitude and the timing of ENSO development. While the composite analysis show no noticeable change.

Contents

1 Introduction

1.1 The effect of season definitions on the simulated paleoclimate

Temporal distribution of insolation, which defines the seasonality of the Earth, has been strongly modulated by the earth's orbital parameters. The changes observed in the seasonality can be attributed to the slow variation in the orbital parameters which affect the amount of solar radiation received at the top of the atmosphere. Pioneering work of Milankovitch (1941) on investigating how the variations of the earth orbital movement affect the solar radiation received at the top of the atmosphere indicated that radiations received by the earth varies with latitude. These variations are considered to be the main driving force for climate change on orbital time scales. Here we introduce these orbital parameters, discuss the variations they undergo:

Eccentricity: The shape of the earth's orbit is known as eccentricity. It measures the discrepancy of the shape of the earth's orbit from being a perfect circle to an ellipse, and therefore reflects the distance between Earth and the sun for a given time. This parameter happens to be the reason for the slightly different length in season for different time periods. For example, summer in the Northern Hemisphere is about 4.5 days longer than winter, spring is about 3 days longer than autumn. When Earth's orbit is most elliptic, the amount of insolation reaching the Earth at its closest approach to the sun is 23% more when compared to its farthest departure from the sun. As Eccentricity decreases, the length of our seasons gradually becomes more equal. Over a period of 100,000 and 400,000 years, the eccentricity varies from 0.0 to 0.0607 as such inducing a small change in the total global annual insolation.

Obliquity: As the earth travels around the sun, the angle at which its axis of rotation is tilted is known as obliquity. Over a period of 400,000 years, the angle has varied between 22^0 and 25^0. Currently, the earth axis is tilted at 23.4^0 and this is slowly decreasing. This is the reason for the more extreme season we observe in the past than present. For example, Larger tilt angle favors periods of deglaciation. However, this effect is not globally uniform as it is latitude-dependent.

Precession: This is described as the slightly wobbling of the earth upon its axis as it rotates. This wobbling is a result of tidal force caused by the gravitational influence of the sun and the moon. Spanning a period of 23,000 years on average, the position of the equinoxes precesses relative to the perihelion causing the change in timing of seasons.

During the past decade, the change of our climate, i.e., global warming, has been the focus of many studies. It is important to state that climate change is not some far-off, future problem we will have to face in a few decades. The reality is, it's happening right now, and threatening. Some questions are still begging for answers, such as what was the climate in the past? Were the seasons observed now exactly the same in the past? What is the effect of these seasons on the climate? How the timing of the seasons affect seasonal mean precipitation and surface temperature? The modeling of paleo-climate and paleo-data can be used to investigate and explain past environment, climate change over full glacial-inter-glacial cycles. Changes in calendar definition can lead to changes in seasonality. More importantly, examining the effect of season definition on simulated paleo-climate can provide answers to the questions earlier raised. Nevertheless, only a few model studies defined the seasonal cycle for the past climate following Kepler's law, and were based on coarse resolution. For example, during the Last Inter-glacial (126 ka B.P.), the time between the vernal equinox and summer solstice was reduced by 4 days compared to present, Summer solstice and Autumnal equinox by 8 days but increment by 4 days between the autumnal equinox and winter solstice, winter solstice and vernal equinox also increased by 8 days. These differences were attributed to the precession of the equinoxes and a larger eccentricity. Studying this change and its impact in seasonal variation, a reference date must be chosen for proper definition of past calendar (months or seasons), following the present day calendar. Usually, March 21 at noon to VE is fixed for any period in the past (for more details, see Joussaume and Braconnot (1997).

Laskar (1993) finds it appropriate to compare values of insolation for the same positions of the earth along its orbit with respect to the VE. Beginning and ending of celestial longitudes are matched for each period on the basis that the number of days in each month and dates of the longitude are relative to the present calendar month set at March 21 (Kutzbach et al., 1998). With all these definitions and over 17 models being run under the approval of the International Geosphere-Biosphere Program and the World Climate Research Program, there have been little or no

study on the definition of season published. However, Laskar (1993) showed a significant difference in insolation computed for two different periods either by using the same astronomical portion or the same date. Moreover, the model studies on the sensitivity of season definitions were mostly based on coarse resolution e.g., Joussaume and Braconnot (1997). It would be interesting to look at the calendar effect in a high resolution setup.

A more recent study by Bartlein and Shafer (2019) has investigated the pure effect of calendar by comparing seasonal cycles of surface air temperature and precipitation of a modern climate state between angular and classical means. The angular calendar corresponding to 6, 97, 116, and 127 ka were applied. Bartlein and Shafer (2019) observed spatial-variable changes in surface air temperature and precipitation as a response to the pure paleo-calendar effect, some of which are very similar to the climate anomalies between paleo and modern climate induced by changes external forcings. Therefore it has been argued that the artificial bias might be interpreted as climatic signal without the correct implementation of season definition.

Various archives have been used for reconstruction of past climate and for evaluating the model's performance in capturing the changes between the past and today's climate. Some proxy such as pollen and speleothem represents only seasonal signal, therefore caution should be taken when comparing proxy records with model output. The use of an angular calendar can ensure the consistency between the time segment represented by the proxy and the model simulation.

1.2 El Nino and the Southern Oscillation

Another sub-topic of the present study is the evolution of El Nino and the Southern Oscillation (ENSO) in a transient Holocene simulation and its impact on the climate at different time intervals. Since analyzing the questions earlier raised, past and future climate projection on how ENSO might react to global warming, how climate change will affect and modify the behavior of ENSO are two important questions and another area of concern taking to the sensitivity of the matter.

ENSO is an energetic and large single source of inter-annual variability of atmosphere–ocean system in the tropics, linked to distant anomalous weather and climate events (such as hurricane occurrences, frequency and severity of tornadoes, droughts, and floods) being termed "teleconnections" e.g., Glantz et al. (1991) and

its impact is greatly felt on the global climate. e.g, (Lau and Nath, 1996, 2003). The amplitude of ENSO can be modulated by various factors e.g., Meehl et al. (2001); Yeh and Kirtman (2005).

A key factor of the interannual variability of ENSO is its influence on seasonal rainfall in the tropics which has undergone and still going through extensive examination since the pioneering studies by Walker in the 1920s where he tried to understand the variations in the Indian monsoon and as well as make predictions (Joly and Voldoire, 2009).

The term 'ENSO' originally has a different meaning which is in the form of a local description of seasonal warm water current that manifest just off the coast of northwestern Peru. Yearly around the Christmas period until February or March, this warm water current replaces the normally cold surface water and the prevailing southerly wind direction reverses. Fishermen off the Peruvian coast named the counter-current 'El Nino' since it tends to arrive at Christmas; the name El Nino is Spanish and it means Christ Child. This local phenomenon is now understood to be part of a more general atmosphere–ocean phenomenon known as the El Nino–Southern Oscillation (ENSO) e.g., Glantz et al. (2001); Allan et al. (1996). After the El Nino of 1891, rains in Peru were huge during the summer of that year.

> The whole coast of Peru was bathed with a massive temperature change due to the hot current from the north leaving a host of Large dead alligators and trunks of trees. Pezet (1895)

This result to the first academic paper on the subject of El Nino Gergis and Fowler (2009) been written, thereby leading to lots of interest

> Variations in tropical Pacific Ocean temperatures and the resulting changes in atmospheric pressure gradients gives a description of ENSO and this atmospheric changes widely propagate the effects of ENSO variability. McPhaden et al. (2006)

The impacts of these changes in regional temperature and precipitation patterns are associated to the phases of ENSO causes a wide range of environmental, societal and economic consequences.Though ENSO is known to be a single climate phenomenon. However, it has three phases:

El Nino Phase: This is the warming of the ocean surface. During this event, trade winds weaken or may even reverse,thus allowing the area of warmer than normal

water associated with a deepening of the thermocline to move into the central and eastern tropical Pacific . The sea surface temperature becomes warmer owning to the contributions of the weaker up-welling of cooler waters from below. Around northern Australia, sea surface temperatures are cooler than normal and the focus of convection migrates away from Australia eastward towards the central tropical Pacific Ocean resulting in increased rainfall over the tropical Pacific Ocean, reduced rainfall over Indonesia and the western Pacific, and for the low-level easterly trade winds near the equator to weaken, possibly enough to change direction and flow west to east.

La Nina Phase: This is the opposing phase to El Nino, the Walker Circulation intensifies with greater convection over the western Pacific and stronger trade winds, resulting in warmer than usual sea surface temperatures in the region north of Australia. Sea surface temperatures across the central and eastern tropical Pacific Ocean become cooler than usual and the thermocline moves closer to the surface as up-welling strengthens. This phases is usually accompanied with rainfall over the tropical Pacific, increased rainfall in Indonesia and the western Pacific, and for the low level easterly winds near the surface to become stronger.During a La Nina year, there are likely-hood that that temperatures in the winter will become cooler and a bit wetter than average in the Northwest, and warmer and drier than average in the Southeast.

The neutral phase: The neutral phase of ENSO involves sea surface temperatures in the tropical Pacific Ocean that are closer to average, with the trade winds blowing easterly across the surface near the equator. The Equator receives great amount of sun rays that warms the Pacific Ocean, thereby bringing warm moist air and warmer surface waters towards the western Pacific and keeping the central Pacific Ocean relatively cool. The warm ocean currents affect the surrounding atmosphere by increasing the temperature and moisture content. Warm air rises high in the atmosphere through convection process causing thundercloud and rain.

Over the years, there are few studies that have looked into ENSO and some aspect of climate relating to it. For example, An and Wang (2000) and Zhang et al. (2008) discussed the possibility of changes in the regularity of ENSO events. But Power and Smith (2007) suggested that during the last few decades, El Nino dominance was as a result of the changes in background state of the Southern Oscillation Index (SOI), instead of variability or shift to more frequent El Nino events alone. Other

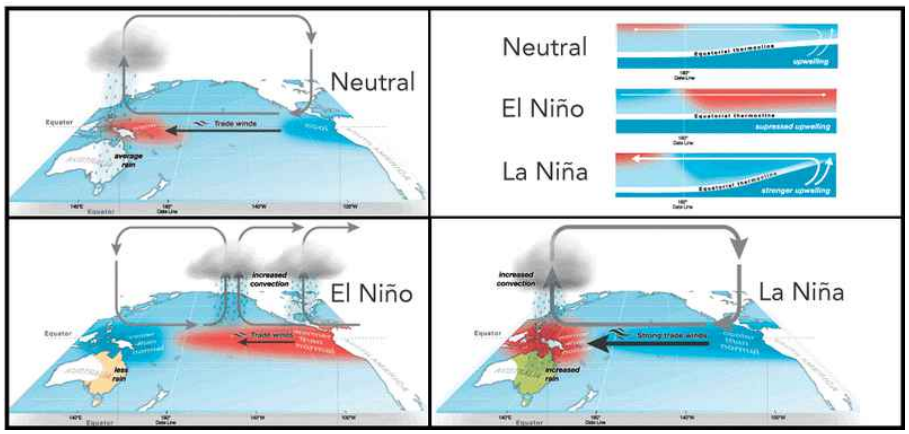

Figure 1: The three phases of ENSO showing the variation of trade wind, convection and rainfall

https://wnyt.com/news/what-is-the-el-nino-southern-oscillation/5895856/

researchers have examined the uncertainty of ENSO in response to climate change as related to uncertainty in model parameters Toniazzo et al. (2008). Another essential part of ENSO is how the teleconnections between the climate variable in many part of the globe vary with time is examined e.g., Trenberth and Caron (2000); Van Oldenborgh and Burgers (2005); Power et al. (2006); Kucharski et al. (2007). Studies has also shown that several ENSO properties such as amplitude, frequency and propagation change from decade to decade e.g., Gu and Philander (1995); Wang (1995); Torrence and Webster (1998); An and Wang (2000), among others.

However, Paleoclimate studies shows that there are evidence indicating past changes in ENSO variability. These changes cannot be dissociated from the differences in the earth orbital parameters as the climate at the mid-Holocene is characterized by an amplification of the seasonal cycle in the Northern Hemisphere and a strengthened summer monsoon activity. Climate model simulations for 6000 years before present (6 ka) by the Paleoclimate Modeling Inter-comparison Project (PMIP) have looked at those aspects by coordinated climate modeling studies (Joussaume and Taylor (1995); Joussaume et al. (1999); Braconnot et al. (2000). Howbeit, these changes in ENSO variability and sensitivity can be noticed by monitoring of ENSO indicator. These indicators include:

Outgoing Long-wave Radiation (OLR): The introduction of continuous satellite-based data in 1979, gave birth to another highly ENSO-relevant index known as outgoing long wave radiation, which indicates the extent of convection (thunder-

storm activity) across the tropical Pacific. By mapping outgoing radiation from cloud tops, detecting areas of the tropical Pacific which experience more rain (dryness) than average. Data gotten are centered across equatorial areas from 160°E - 160°W longitude, 5°S - 5°N Longitude.This raw data are converted into a standardized anomaly index. Areas having sea surface temperature above-average experience thunderstorm activity often (not always). The outgoing longwave radiation is therefore not only very relevant to the ENSO state, but also serves as a key linkage to the remote climate teleconnections outside the tropical Pacific region. e.g., Chiodi and Harrison (2013)
Southern Oscillation Index (SOI): This is one measure of the large-scale fluctuations in air pressure occurring between the western and eastern tropical Pacific (i.e., the state of the Southern Oscillation) during El Nino and La Nina episodes. Traditionally, this index has been calculated based on the differences in air pressure anomaly between weather station of Tahiti and Darwin, Australia (Tahiti minus Darwin) (Troup (1965); Torrence and Webster (1999)). However, an El Nino event is consistent with a pressure above average condition in Darwin and pressure below average condition in Tahiti indicating a negative SOI value while the opposite conditions , a positive SOI value.

In an effort to achieve thoroughness and greater compatibility with a gridded dataset over single point weather stations, the Equatorial Southern Oscillation Index (ESOI) was developed to measure ENSO intensity. NOAA refined the original SOI index by using the standardized difference in average sea level pressure over two large regions centered on the equator (5°S - 5°N) over Indonesia (90 - 140°E) and the eastern Pacific (230 - 280°E) (Pacific minus Indonesia) Barnston (2015), NOAA Climate.gov; "Southern Oscillation Index (SOI) and Equatorial SOI", International Research Institute for Climate and Society, Columbia University)

The ESOI index is superior for using average SLP over two large regions centered on the equator equator (5°S - 5°N) over Indonesia and the eastern equatorial Pacific (as seen in the RHS of Fig 2), where the majority of the ENSO signal manifests. This makes it possible to solve the problem of shorter term fluctuations unrelated to ENSO and the limitation of Southern Oscillation Index where both Tahiti and Darwin are located a little south of the equator (Tahiti at 18°S, Darwin at 12°S).

Sea Surface Temperature (SST): The commonly used ENSO indices today are sea surface temperature (SST)-based indices which measure anomalies to climatology

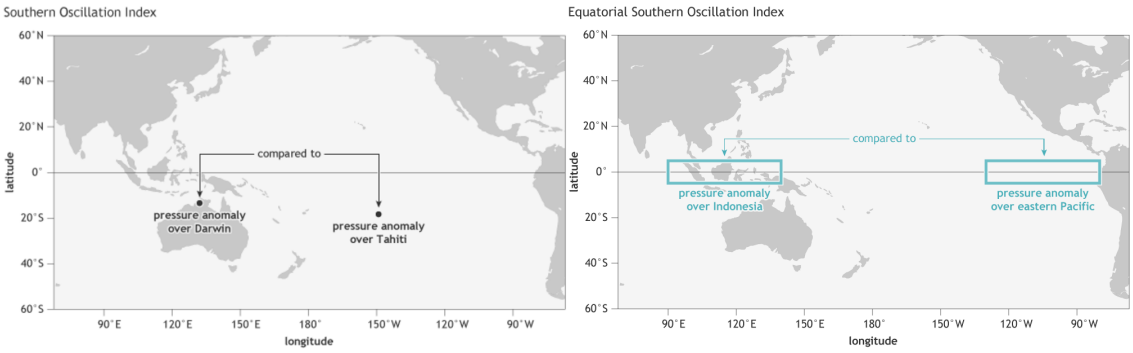

Figure 2: SOI weather stations and ESOI regions. Taken from Barnston (2015), NOAA Climate.gov.
https://www.climate.gov/news-features/blogs/enso/why-are-there-so-many-enso-indexes-instead-just-one

averaged over some defined regions of the equatorial Pacific. Base on the work of Dr. Kevin Trenberth (Trenberth, 1997; Trenberth and Stepaniak, 2001), four Nino regions have been defined and classified by the National Center for Atmospheric Research (NCAR), the University Corporation for Atmospheric Research (UCAR), and the National Oceanic and Atmospheric Administration (NOAA). These region identified as Nino 1, 2, 3, and 4 regions correspond to labels assigned to ship tracks historically, simplifying the effort to construct historic records of El Nino back to 1949 (Rasmusson and Carpenter, 1982).

The Nino 1 and 2 regions (now combined to a single "1+2" region) make up the smallest and eastern-most regions of study of Nino SST variations. These regions are found on the west coast of South America (0 - 10°S, 90°W - 80°W), where El Nino events was first recognized by the local residents and have the largest variance of all Nino SST indices. So this region typically warms first in the event of an El Nino.

The Nino 3 region (5°N - 5°S, 150°W - 90°W) was historically the accepted region for monitoring and predicting ENSO events, but research later showed that it is the most predictive region for coupled ocean-atmosphere interactions lying further to the west (Trenberth, 1997).

The Nino 4 region (5°S - 5°N, 160°E - 150°W) was eventually developed and it happened to show the least variance of all SST indices. however it is the latest Nino "3.4" region (5°N - 5°S, 170°W - 120°W) that is most widely accepted today.

The Nino 3.4 (5°N - 5°S, 170°W - 120°W) region is most widely accepted because it can better represent the average equatorial SST anomalies across the Pacific,

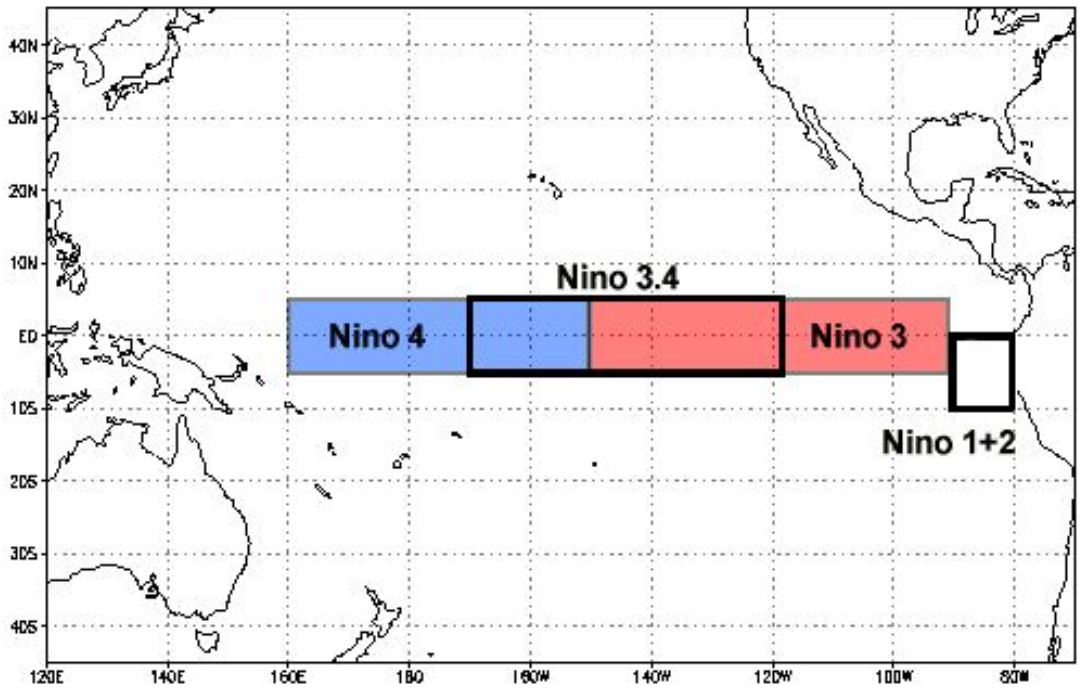

Figure 3: Most commonly used regions to study track ENSO by way of area-averaged SST anomalies.
https://climatedataguide.ucar.edu/climate-data/nino-sst-indices-nino-12-3-34-4-oni-and-tni

including parts of both the Nino 3 and 4 regions ("Nino SST Indices", NCAR UCAR Climate Data Guide) and it is for this reason, we will be exploring the Nino 3.4 regions as indices of ENSO intensity. Trenberth (1997) encourages the use of the 1950-1979 period as the climatology against which to calculate SST anomalies, as the period from 1979 to 1997 appeared to be dominated by warm events.

Index	**Lat range**	**Lon range**
Nino-1+2	0-10°S	90-80°W
Nino-3	5°N-5°S	150-90°W
Nino-3.4	5°N-5°S	170-120°W
Nino-4	5°N-5°S	160°E-150°W

Table 1: The Lat and Lon ranges defining area averages for SST indices

.

Oceanic Nino Index (ONI): The Oceanic Nino Index (ONI) is NOAA's primary indicator for monitoring and defining the phase of ENSO events which has significant teleconnections all around the globe. This simple index calculates a 3-month

running mean (3-MRMs) of SST anomalies in the Nino 3.4 region based on a climatology of a centered 30-year period updated every 5 years. The updating of the base periods is done to remove the observed warming trend in the Nino 3.4 region.

Researchers identified an ONI SST-related statistical 3-MRM threshold of ≥ 0.5°Celsius for the likely onset of El Nino's anomalous SST warming that would remain above that certain threshold for several months. To qualify officially as an El Nino episode, the SST anomaly must continue at ≥ 0.5°Celsius or higher for a total of 5 consecutive 3-month running means (3-MRMs) (NOAA 2019b). This period of time encompasses 7 consecutive months. An event of $\pm$ 0.5°Celsius is used to signal an El Nino or La Nina event, respectively (Dahlman, 2016). Again, positive values of the index indicate an El Nino event, while negative values indicate a La Nina event.

Nevertheless, Paleoclimate studies using proxy data acknowledge weaker ENSO variability in the mid-Holocene (e.g., Gagan et al. (1998); Tudhope et al. (2001); Cole (2001); McGregor and Gagan (2004); Rein et al. (2005). El Nino variability experience a reduction in the Holocene as established by Liu et al. (2000) modeling study. While Otto-Bliesner (1999) obtained comparable SST variability in the eastern equatorial Pacific at 6 ka compared to that at the present. Using a simple coupled model, Clement et al. (2000) simulated weaker ENSO activity in the mid-Holocene than in the present. Otto-Bliesner et al. (2003), using the National Center for Atmospheric Research (NCAR) Climate System Model (CSM), obtained weaker ENSO for the Holocene and stronger ENSO for the Last Glacial Maximum (LGM). Attributing the weaker ENSO to a strengthening of the tropical Pacific trade winds and weakening of the tropical thermocline. Otto-Bliesner et al. (2006) recent modeling study with CCSM3 shows weaker ENSO variability for both the Holocene and LGM. Having all these paleo-ENSO simulation studies can really give us a chance to understanding and observing the mechanism of ENSO variability and its changes, as much as providing useful suggestion for future ENSO changes by the ever increasing anthropogenic greenhouse gases.

This thesis aims to briefly show us the calendar effect in both time-slice (a pre-industrial control experiment (PI), as well as two paleo runs: mid-Holocene (MH) and Last Inter-glacial (LIG)) and transient simulations (applying boundary conditions of the past 6,000 years), with a focus on the surface temperature and pre-

cipitation. Not withstanding examining calendar effect on magnified large-scale climate patterns like the El Nino and the Southern Oscillation (ENSO), showing the response of monsoon to ENSO through time (i.e 6-5k, 5-4k, 4-3k, 3-2k, 2-1k and 1-0k) using transient simulations.

Advancing our study can not be overemphasized hence the need for the high resolution model for better understanding of the climate evolution for the transient simulations. This paper is written in the following order. Section 2 deals with the model and method employed which includes the coupled climate model: AWI-ESM; tools for data analysis: CDO, NCL and Super-computer Mistral. We also describe how we performed the calendar correction and a little explanation of the configuration deployed in our experiments and performed simulations to get the actual NINO3.4 index. Section 3 shows preliminary results and discussion on the anomalies for the surface temperature and precipitation for the periods anticipated. Also showing the result for the Variability, Sensitivity, Composite analysis in response of monsoon to ENSO through time. section 4 we give conclusions and summary of this study.

2 Methodology

2.1 Model description: AWI-ESM1 and AWI-ESM2

The first version of Alfred Wegener Institute (AWI) Earth System Model (AWI-ESM1) is a state-of-the-art coupled climate model based on the finite element formulation. It is suitable for application in simulating modern background climates (Danilov et al., 2017; Sidorenko et al., 2019). This model comprises the atmospheric component ECHAM6 with includes a vegetation module JSBACH, and the ocean-sea ice component FESOM1.4 which is based on the finite element formulation. AWI-ESM1 employs the OASIS3-MCT coupler (Valcke, 2013) with an intermediate regular exchange grid. Mapping between the intermediate grid and the atmospheric/oceanic grid is handled with bilinear interpolation. The atmosphere component computes 12 air–sea fluxes based on four surface fields provided by the ocean module FESOM1.4. A newly developed model version AWI-ESM2 has the same atmospheric module ECHAM6 as used in AWI-ESM1, but a different ice-ocean component FESOM2.0 (Sidorenko et al., 2019). The AWI-ESM1 has proven to be a useful tool following series of simulations which have been undertaken, including the studies of the past and future simulations of ENSO (Brown et al., 2020), the mid-Holocene (Shi and Lohmann, 2016; Brierley et al., 2020), the early-Holocene (Shi et al., 2020), the Last Interglacial (Kageyama et al., 2020b; Otto-Bliesner et al., 2020), and the Last Glacial Maximum (Renoult et al., 2020; Lohmann et al., 2020; Kageyama et al., 2020a). Here we turn to introduce both atmosphere and ocean components as mentioned above.

2.1.1 The Atmospheric Model ECHAM6

The atmospheric model ECHAM6, is the most recent version of the ECHAM model developed at the Max Planck Institute for Meteorology (MPI) in Hamburg. ECHAM6 was developed to contribute to the institute's support in the sixth phase of the coupled model inter-comparison project (CMIP). It is focused on coupling between diabetic processes, constantly associated with small-scale fluid dynamics and large-scale circulations. The model is branched from an early release of the European Center (EC) for Medium Range Weather Forecasts (ECMWF) model (Stevens et al., 2013). ECHAM6 dynamics is based on hydrostatic primitive equations (HPEs) with traditional approximation. The Gaussian grid used in the model is to calculate nonlinear equation terms and some physical representation. The

configuration of boundary layer and turbulence is based on eddy diffusivity and viscosity approach. Momentum transport arising from boundary effects is configured using the subgrid orography scheme as described by Lott (1999). Subgrid-scale cloudiness assume the role of humidity distribution function scheme developed by Sundqvist et al. (1989). Radiative transfer in ECHAM6 is represented by the rapid radiation transfer (Iacono et al., 2008) containing a Land-Surface Model (JSBACH) which includes 12 functional plant types of dynamic vegetation and 2 bare-surface types (Loveland et al., 2000; Raddatz et al., 2007). The development of ECHAM6 is such that it runs a high priced vertical grid of 47 or 95 vertical levels, and horizontal resolutions ranging from T31 to T255 which can be seen from the table below;

Name	**Levels**	**Description**
CR	T031L47	Instruction purpose (also can run at L31)
LR	T063L47	Default resolution (GR15 Ocean land mask)
MR	T063L95	High resolved middle atmosphere (TP04 Ocean land mask)
HR	T127L95	High resolution
XR	T255L95	Experimental very high resolution

Table 2: Model Resolutions

2.1.2 FESOM1.4

The sea-ice ocean component in the coupled system is represented by Finite element sea-ice ocean circulation model, FESOM which allows for simulating ocean and sea ice dynamics on unstructured/vague meshes with variable resolutions. Is characterized by the possibility of refining areas of particular interest in the global setting, resolving narrow straits when needed and allowing for a smooth representation of coastlines and bottom topography. FESOM happen to have been proved in numerous studies with prescribed atmospheric forcing see e.g., Sidorenko et al. (2011), Danabasoglu et al. (2014), Wang et al. (2013).

Though a competitive tool for studying the ocean general circulation, it's numeric are basically different from the frequently-grid model. The basic principle are described by Timmermann et al. (2009), Wang et al. (2013), Danilov et al. (2017). However, some characteristic makes it a standout. For example, a spherical coordinate system with the poles over Greenland and the Antarctic continent to avoid convergence of meridians in the computational domain. The normal resolution of

150km in the open ocean is gradually refined to about 34km in the Northern north Atlantic and tropics.

In conclusion, FESOM runs with a linear free surface and the 3-dimensional mesh is formed by vertically extending the surface grid using 47 unevenly spaced z-levels and the ocean bottom is represented with shaved cells.

2.1.3 FESOM2.0

The new version of the Finite element sea-ice ocean circulation model FESOM2.0 is based on the finite volume discretization which is formulated on unstructured meshes and offers multi-resolution functionality in a faultless and flawless ways. The impact of local dynamics on the global ocean is related to a number of FESOM-based studies see Danilov et al. (2017) indicate that the multi-resolution approach advocated by FESOM is successful and allows one to explore the impact of local processes on the global ocean with moderate computational effort see Danilov et al. (2017). In a bit to explore ways further increase the numerical efficiency of unstructured mesh and extend their area of applicability, FESOM2.0 was birthed.

Sidorenko et al. (2019) presented many details on the finite volume method used by FESOM2.0. However, the performance of FESOM2.0 is compared to that of FESOM1.4 in simulation driven by the CORE-II forcing (Large and Yeager, 2009), reports has it that the simulations carried out on a coarse mesh used by FESOM1.4 in the frame work of CORE-II inter-comparison and on global mesh with a resolution of about 15km, illustrating it to be a fully functional and highly competitive general ocean circulation model. This new version improves the numerical efficiency of FESOM in terms of CPU time by at least 3 times while retaining it's fidelity in simulating sea-ice and the ocean.

2.2 Tools used for model

2.2.1 The Climate Data Operators (CDO)

CDO is an application with multiple threads in a shared address space which offers a scripting interface for Ruby and Python. This software contains more than 700 operators used for the executing of standard climate and forecast model data. The operators include simple statistical and arithmetic functions, data selection and sub-sampling tools, and spatial interpolation. Having been developed to be a one

package with same set of processing functions for GRIB and NetCDF, it possess the characteristics of been a simple UNIX command line interface, extendable modular design with new operators, speedy processing of large datasets, supporting many different grids types, handling datasets of operators with missing values and the option of not storing the interim results in files of dataset processed by several operators etc.

2.2.2 NCAR Command Language (NCL)

The NCL is a free interpreted language invented specially for scientific data processing and visualization. Sponsored by the National Science Foundation and a product of the Computational & Information Systems Laboratory at the National Center for Atmospheric Research NCAR. It runs in interactive mode, interpreting each line as it is entered at your workstation, or in batch mode acting as an interpreter of complete scripts and using command line options to set options or variables. Utilizing this language power is evident in file input and output, data analysis and visualization.

2.2.3 Super-computer Mistral

Super-computers are essential for effective and efficient running of model simulations. These super-computers carry out all calculations faster, dedicating enough space to the operator for assessments and applications. In the present study, we performed our simulations based a super-computer platform called Mistral. Mistral is a high performance computer system for Earth System Research 3 (HLRE-3) at the German Climate Computing Center in Hamburg, DKRZ.
https://www.dkrz.de/systems/hpc/hlre-3-mistral

Figure 4: Mistral Super computer

2.3 Experimental Design

For any simulation to be successful, it must be based on a particular geologic period and the model initiated to carry out this simulations must be adjusted according to the period's characteristics, which include greenhouse gas concentration, orbital parameters and geography patterns.
Using the circulation model AWI-ESM1 at a high oceanic resolution up to 20 km in polar oceans and coastal regions, we have performed several time-slice experiments: a pre-industrial control experiment (PI), as well as two paleo runs: mid-Holocene (MH) and Last Inter-glacial (LIG), by prescribing the appropriate boundary conditions shown in Table 3. In MH and LIG, the topography and ice-sheet properties are kept the same as in the PI control experiment. All time-slice experiments are initialized from the same initial condition and have been integrated for more than 1,000 simulation years, and the output from the last 100 years were used for analysis. (Kageyama et al., 2017).

Moreover, one transient experiment was conducted using AWI-ESM2, which applied the boundary conditions of the past 6,000 years. Orbital parameters are calculated according to Berger (1978), the greenhouse gases are taken from ice-core records and from recent measurements of firn air and atmospheric samples (Köhler et al., 2017). See Vorrath et al. (2020) for more information.

2.4 Analysis on El Nino and the Southern Oscillation

In this study, useful indices of ENSO are needed, which are calculated as the sea surface temperature (SST) anomalies over the Nino3.4 region, i.e., 5N-5S, 170W-120W. The Nino3.4 indices have been thought of as representing the average equatorial sea surface temperatures across the Pacific from about the dateline to the South American coast, this is the reason why we choose Nino 3.4 regions to derive the ENSO intensity and variance. Trends will be then removed from the time series of Nino3.4 using CDO and NCL. Here we focus on the simulated evolution of seasonality and interannual variability of ENSO throughout the past 6000 years, as well as the effect of ENSO on climate variables at different time intervals. According to Carré et al. (2021), seasonality is here defined as the averaged amplitude of the annual cycle (maximum monthly Nino3.4 index minus minimum monthly Nino3.4 index in a calendar year). The interannual variability is calculated as the variance of the annual mean Nino3.4 index after filtering out low frequency variability (>10 years). A running mean factor of 100 years is then applied to the computed time series of seasonality and interannual variability to derive their centennial-scale evolution. In addition, composite analysis is performed to investigate the ENSO teleconnection patterns, on both global and regional spatial scales, which will be identified in the course of this study.

Table 3: Boundary Conditions employed by the model for the period under investigation.

Experiment	**Last Interglacial (LIG)**	**Preindustrial (PI)**	**Mid-Holocene (MH)**
Orbital Parameters			
Eccentricity	0.039378	0.016764	0.018682
Obliquity (degrees)	24.040	23.459	24.105
Perihelion-180 °	275.41	100.33	0.87
Vernal equinox	Fixed to noon on March 21	Fixed to noon on March 21	Fixed to noon on March
Greenhouse Gases			
Carbon dioxide (ppm)	275	284.3	264.4
Methane (ppb)	685	808.2	597
Nitrous oxide (ppb)	255	273	262
Other characteristics			
Solar constant (W/m^2)	Same as PI	1360.747	Same as PI
Paleogeography	Same as PI	Modern	Same as PI
Ice sheets	Same as PI	Modern	Same as PI

2.5 Calendar correction

It is imperative to note that the seasons defined based on classical "fixed-day" calendar do not match up with the astronomical seasons which correspond to 90^0 segments of the Earth's position along its orbit (Timm et al., 2008). Applying today's fixed-day calendar to past annual cycles can lead to notable biases, as evidenced in various previous studies (Bartlein and Shafer, 2019; Joussaume and Braconnot, 1997; Timm et al., 2008) hence a calendar correction should be applied for the purpose of the experiment. Observing the changes in the earth's orbital parameter over time, the induced change in the amount of annual mean total insolation received by the Earth can be attributed to the slow variation in eccentricity from nearly 0 to 0.0607. Obliquity oscillates from 22^0 to 25^0 and the position of the equinoxes precesses relative to the perihelion all over some period of time. It is important to take these changes into consideration hence the need to define a reasonable calendar for the past. When defining seasons contained in a 12-month calendar with its respective configuration, it is important to compare seasonal climate to the earth's position along its orbit.

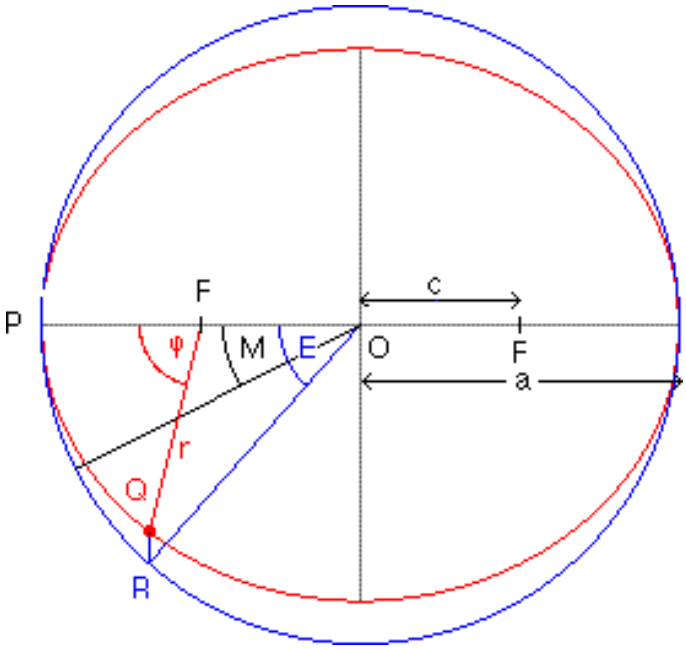

Figure 5: The mean, eccentric and true anomaly. Here stands for the true anomaly, defined as the angle between the perihelion on the major axis of the orbit ellipsoid and the current position of earth; M the mean anomaly, i.e. the angle between the perihelion and earth's position based on the assumption that the orbit would be a perfect circle; and E the eccentric anomaly, which is an angular parameter that defines the position of a body that is moving along an elliptic Kepler orbit. F is the position of the Sun and Q the position of the Earth. P represents the position of perihelion.

.

The angle between the perihelion on the major axis of the orbit ellipsis and the Earth's current position defines the Earth's true anomaly while a month is defined as a 30^0 increment of the true longitude seen from a fixed position. This fixed position is usually the Northern Hemisphere vernal equinox which is set at March 21st corresponding to 81 in the classical calendar year as earlier stated. In the following we describe how we perform the conversion from classical fixed-length calendar to an angular one.

As mentioned above, we define Earth's true anomaly θ as the angle between the perihelion on the major axis of the orbit ellipsis and the Earth's current position. Between perihelion and aphelion, there are two points, which are the so-called spring and autumn vernal equinox, at which the the Sun is exactly above the Equator and day and night on Earth are of equal length. Here we fix the spring vernal equinox as March 21st, which serves as a starting point. We then define a month and season as a 30^0 and 90^0 increment of the true anomaly θ , respectively.

By doing so, we can compute the starting-point and end-point of each month (season) via an angle 30^0 (90^0). In order to define an angular calendar, we then need to calculate the lengths of months (seasons) by computing how much time the Earth needs to move from the respective starting-point to the end-point of a month (season). Here we then obtain a connection between θ and the time elapsed since Earth passed perihelion. We assume that the Earth's orbit is a perfect circle, and we can then define a mean anomaly M as the angle between the perihelion and Earth's position as:

$$M = \frac{2\pi}{T} \cdot t_p \tag{1}$$

Here, t_p stands for the time elapsed since Earth passes the perihelion and T denotes the orbital period (i.e., 365 days). Considering the eccentricity of the Earth's orbit ϵ, we calculate the eccentric anomaly E via:

$$E - \epsilon \cdot \sin(E) = M \tag{2}$$

The application of Newton's method can help to solve the above equation (Danby and Burkardt, 1983). Then we have:

$$\theta = 2 \cdot \arctan\left(\sqrt{\frac{1+\epsilon}{1-\epsilon}} \cdot \tan\left(\frac{E}{2}\right)\right) \tag{3}$$

By the above equations, we obtain a concrete relationship between t_p and the true anomaly θ. Then we are able to obtain the starting and end date of each month and season.

3 Results

3.1 Shift of months/seasons between classical and angular calendars

Based on the approach illustrated in the previous section, we calculated time-range of each season for angular calendar for two paleo time periods: mid-Holocene and last interglacial, as well as for pre-industrial state. Note that for the pre-industrial,

the fixed-length calendar used in present-day is not an angular calendar, though very similar, and therefore also needs to be converted. The results are shown in table 4

From Table 4, non-ignorable differences in the months and season between the two calendars should be noted: January in PI has 2 days shift in the Angular calendar as compared to the classical calendar while in MH, it happens to be a zero day shift. February in PI has -2 days shift in angular calendar compared to the classical calendar while in the MH, it is -3 days shift. However for PI, the shift of days in Angular calendar as compared to Classical calendar ranges from -1 to 2 days while for MH, it ranges from -3 to 1 day shift. The seasons are not spared also but significantly, the number of winter days are fewer while summer days are more which is represented in both Angular and Classical calendar. For PI in the angular DJF and JJA has 89 days and 92 days, while the classical DJF and JJA has 90 and 92 days respectively. But there is a contrast to the norm in MH where DJF and MAM in the angular calendar has longer days than the classical calendar while JJA and SON are shorter but the shortest season happen to be 85 days which is JJA in the LIG. For more detailed information, we refer to Table 4.

3.2 The effect of season definitions on the simulated paleoclimate

In order to evaluate the calendar effect, we converted the calendar for all of the three equilibrium simulations performed with AWI-ESM1, i.e., PI, MH and LIG, using the approach described in the previous section. For each simulation, the anomalies in surface air temperature, as well as in precipitation, in angular means as compared to classical means, are analyzed. Furthermore, we also investigate the calendar effect on the simulated anomalies between paleo and modern climate states (i.e., MH minus PI and LIG minus PI). It would be interesting to find out to what extent the calendar-induced bias is misinterpreted as climatic signal with the implementation of classical fix-day calendar.

Table 4: Starting and end date of Angular month in PI, MH and LIG, referencing to today's fix-day calendar in a no-leap year. Note that today's calendar is not an angular calendar and should be corrected as well.

Month/Season	PI	MH	LIG
Jan.	02Jan.-30Jan.	29Dec.-28Jan.	26Dec.-27Jan.
Feb.	31Jan.-01Mar.	29Jan.-28Feb.	28Jan.-28Feb.
Mar.	02Mar.-31Mar.	01Mar.-31Mar.	01Mar.-31Mar.
Apr.	01Apr.-01May.	01Apr.-02May.	01Apr.-30Apr.
May.	02May.-01Jun.	03May.-02Jun.	01May.-29May.
Jun.	02Jun.-02Jul.	03Jun.-03Jul.	30May.-26Jun.
Jul.	03Jul.-02Aug.	04Jul.-02Aug.	27Jun.-24Jul.
Aug.	03Aug.-02Sep.	03Aug.-01Sep.	25Jul.-22Aug.
Sep.	03Sep.-03Oct.	02Sep.-30Sep.	23Aug.-20Sep.
Oct.	04Oct.-02Nov.	01Oct.-29Oct.	21Sep.-21Oct.
Nov.	03Nov.-02Dec.	30Oct.-28Nov.	22Oct.-22Nov.
Dec.	03Dec.-01Jan.	29Nov.-28Dec.	23Nov.-25Dec.
Winter	03Dec.-01Mar. (89)	29Nov.-28Feb. (92)	23Nov.-28Feb. (98)
Spring	02Mar.-01Jun. (92)	01Mar.-02Jun. (94)	01Mar.-29May. (90)
Summer	02Jun.-02Sep. (93)	03Jun.-01Sep. (91)	30May.-22Aug. (85)
Autumn	03Sep.-02Dec. (91)	02Sep.-28Nov. (88)	23Aug.-22Nov. (92)

3.2.1 Mid-Holocene

The mid-Holocene (6k) is one of the key times in the past. The most prominent difference between 6k and present arises from the orbital configuration and concentrations of greenhouse gases. Due to the differences in orbital parameters, there is more annual mean solar radiation than today in 6k which interprets that the mean climate should be warmer than today. As shown in Fig. 6, in general, the boreal autumn (SON) over the Arctic region receives much more insolation in 6k compared to pre-industrial, with the anomaly being over 60 w/m^2. While the opposite case is for the Arctic winter time, in which the mid-Holocene gets 30 w/m^2 less solar insolation. For the Antarctic, the insolation difference is positive in JJA and negative during SON. Over the regions of the tropical and sub-tropicals, there is a general positive anomaly of insolation during boreal summer and the opposite case for boreal winter. For the yearly mean, the Arctic receives more radiation and tropics less in 6k with regards to present-day. But for global average, the radiation is actually more in 6K than in the present. Due to the above mentioned insolation difference, the seasonality for the mid-Holocene is larger than today which means that summer is warmer and winter is colder.

As shown in Fig. 7, there is a general warming over the North Hemisphere continents

in boreal summer and autumn. However, the winter temperature there experienced a cooling compared to present-day. This is consistent with the insolation anomaly over Northern Hemisphere sub-polar and sub-tropical regions. The Antarctic was colder in DJF and MAM, and warmer in JJA and SON, which is also in agreement with the insolation changes shown in Fig. 6. In Africa, the Sahel desert, it was colder in winter and summer and the reason was because in the 6K, Sahel was covered with lots of vegetation. The combined effects from increased vegetation and the clouds in the 6k over Sahel leads to the cooling. For precipitation, the Sahel region not just Africa but North America and Asia all experienced more rainfall in the 6K. The monsoon precipitation over Northern Hemisphere was much heavier in the 6K. This is because the position of the Intertropical Convergence Zone (ITCZ) was more to the north than today (Fig. 8). Again due to the changes in orbital parameters, in the 6k the Northern Hemisphere is warmer in boreal summer months, therefore the location of the maximum temperature over the tropical belt shifted northward, as a consequence, the center of the ascending air also migrate to the north, which explains the northward displacement of the mid-Holocene ITCZ.

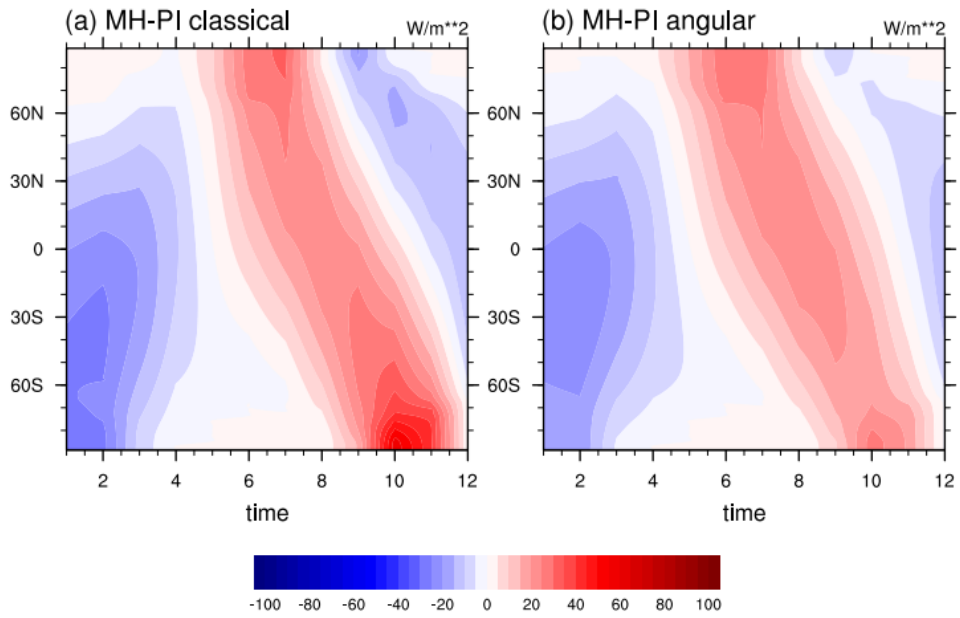

Figure 6: Difference of top-of-atmosphere insolation between 6k and 0k performed by AWI-ESM1 for (a) classical calendar and (b) angular calendar.

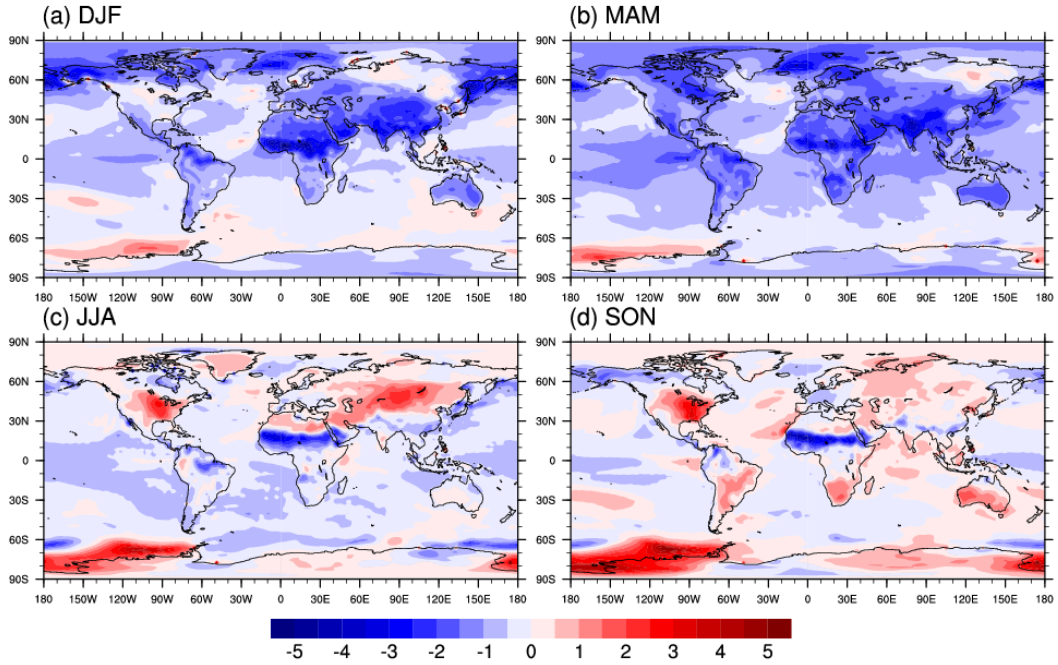

Figure 7: Temperature anomalies between mid-Holocene and pre-industrial performed by AWI-ESM1 for (a) DJF, (b) MAM, (c) JJA, and (d) SON under standard calendar.

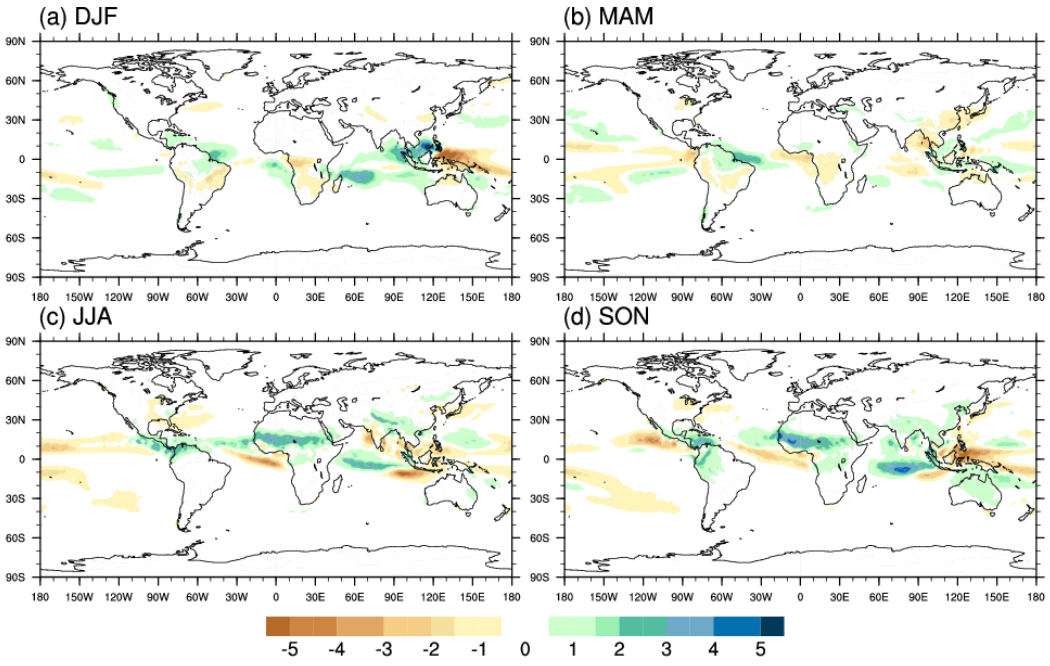

Figure 8: Preciptation anomalies between mid-Holocene and pre-industrial performed by AWI-ESM1 for (a) DJF, (b) MAM, (c) JJA, and (d) SON under standard calendar

In Fig. 9 we depict the responses in mid-Holocene surface temperature to calendar conversion. We observe that there is an overall warming over the Northern Hemisphere and cooling over the Southern Hemisphere, except the warming over Antarctic continent during DJF. In general, the changes are more pronounced over continents than oceans. The most pronounced change happens over North America subpolar area, with a warming being up to 0.5 K. The Southern Ocean shows a significant cooling of up to -0.3 K. Note that the Sahal region shows a cooling in JJA, in consistent to a stronger simulated rainfall there after calendar correction. Overall, we find an overall di-pole pattern of calendar effect on the 6k surface air temperature in each season. Another thing to be noted is that the response in 6k surface air temperature to conversion of calendar is spatially variable, with relatively more pronounced changes at mid-to-high latitudes for both hemispheres and relatively smaller changes over low latitudes (except North Africa). Moreover, we also observe a distinct contrast between the land and the ocean, with the anomalies over continents being much more pronounced than that over the oceans. This could be associated with the much higher heat capacity of the sea water as compared to that of the land, therefore the land surface is more sensitive to changes in the incoming insolation between the two calendars. It should be note here physically the insolation at the 6k itself does not change, just the calculated mean incoming insolation averaged over each season, which might begin and end at a different date when using different calendars, changes. This finally leads to the "computed" temperature anomalies between the two calendars.

Fig. 10 represents the responses of surface air temperature in PI to calendar conversion. The most pronounced difference can be found in boreal autumn, with the anomalies being up to -0.6 K and 0.5 K over Northern and Southern Hemisphere respectively. For the Northern Hemisphere the maximum anomaly value happens over northeastern Asia as well as North America, while for the Southern Hemisphere the maximum response in surface air temperature occurs over the Antarctic continent. For other seasons, only slight differences could be seen. In DJF we observe a negative anomaly up to -0.2 K over Northern Hemisphere continents and a positive anomaly within 0.2 K over the Antarctica. In boreal spring, the change of temperature is up to 0.3 K for the Arctic Ocean and the subpolar continents of the Northern Hemisphere. For the remaining areas the changes can be ignored. In JJA the temperature response to calendar effect is very non-uniform, but in general we observe a slight warming for Northern Hemisphere oceans and a slight cooling over

Southern Hemisphere oceans and Antarctica.

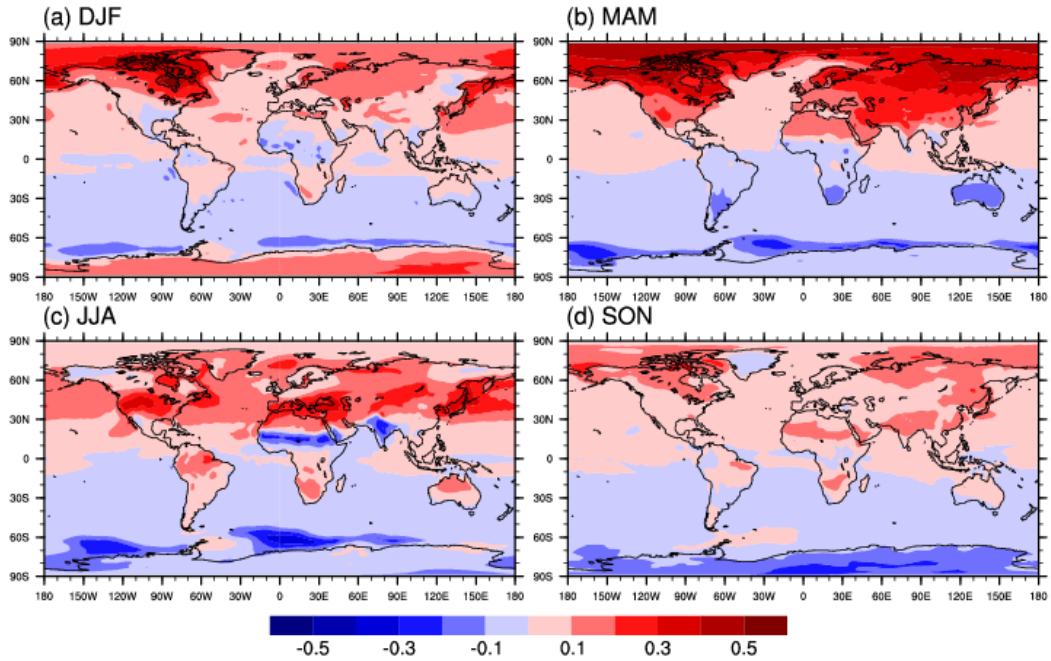

Figure 9: Mid-Holocene temperature anomalies between angular and classical means performed by AWI-ESM1 for (a) DJF, (b) MAM, (c) JJA, and (d) SON.

Since in present-day, there is only little difference between classical and angular calendars (Fig. 10), especially for boreal winter, spring and summer, therefore the pattern described in Fig. 9 mostly dominates the differences in temperature anomalies (6k-0k) between angular and classical means (Fig. 11). The most significant changes occur in boreal autumn, with a pronounced warming over the Northern Hemisphere of up to 1K. There are two reasons contributing to such change, on one hand, the angular-minus-classical means for MH in SON show a general dipole pattern with warming and cooling over Northern and Southern Hemisphere respectively, while on the other hand, such pattern is reversed for PI. Another interesting pattern is the cooling of up to -0.6K over the Antarctic. This mostly reflect the shift of the SON days in the two time periods: in mid-Holocene the boreal autumn lasts 88 days starting from 2nd September in classical calendar, 3 days shorter as present-day calendar.

For other seasons, there are relatively less pronounced changes in the MH-minus-PI anomalies, but they are non-ignorable. For example the warming over North America in DJF is worth noted with a magnitude of 0.5 K, which could be interpreted as climatic signal if angular means are not considered. In general DJF

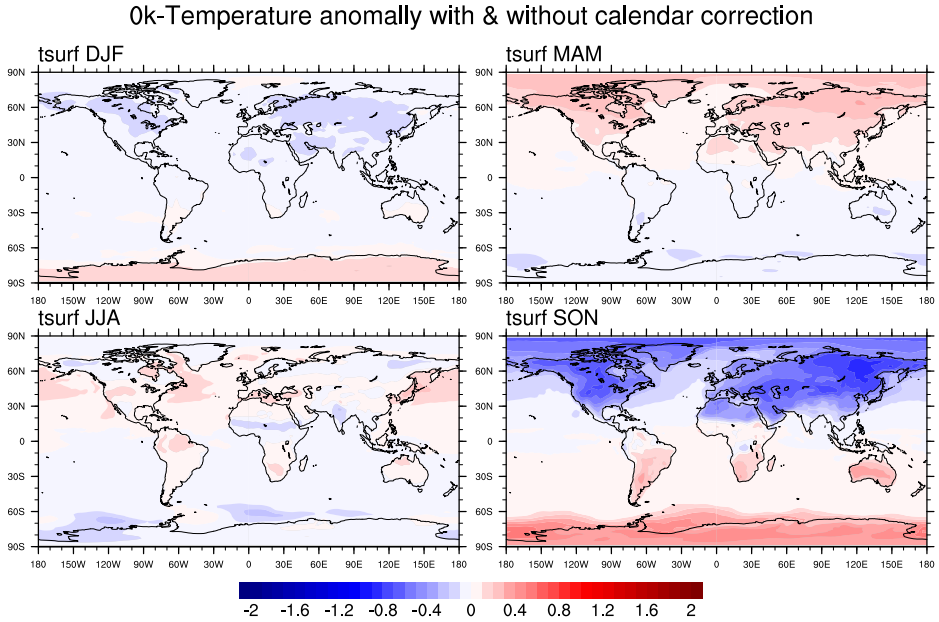

Figure 10: Pre-industrial temperature anomalies between angular and classical means performed by AWI-ESM1 for (a) DJF, (b) MAM, (c) JJA, and (d) SON.

presents a warming over Northern Hemisphere and Antarctica, while a cooling over the remaining regions. Similar pattern could be seen for boreal spring, but with less pronounced responses. In JJA, the most notable pattern is the warming over Northern Hemisphere continents up to 0.3 K, which means a cooling bias in the classical MH-minus-PI temperatures.

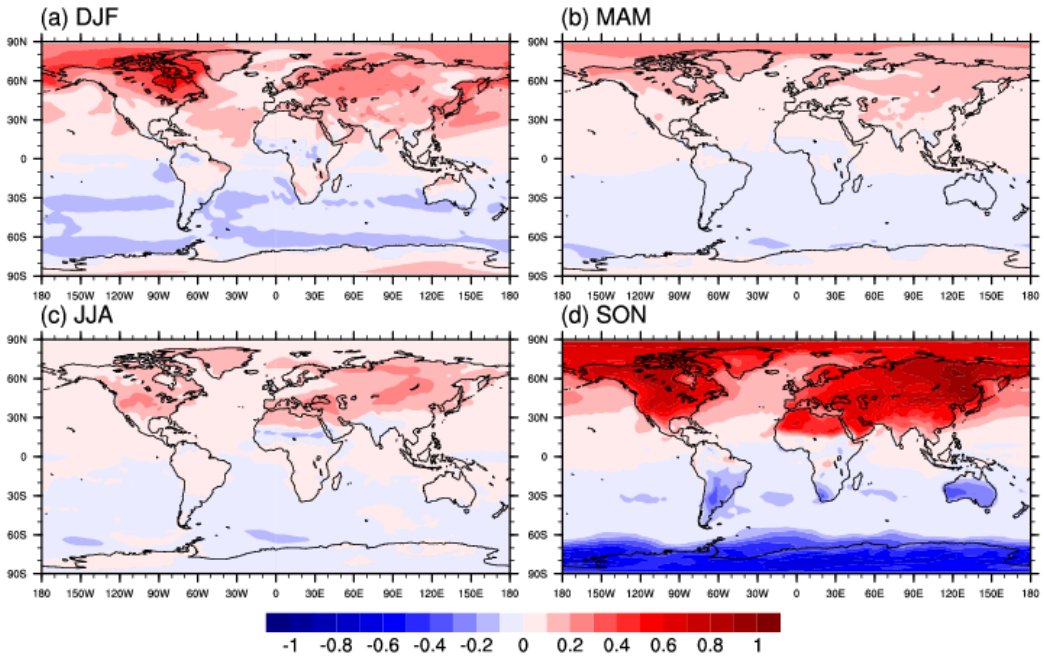

Figure 11: Differences in temperature anomalies (6k-0k) between angular and classical means performed by AWI-ESM1 for (a) DJF, (b) MAM, (c) JJA, and (d) SON.

Mid-Holocene precipitation anomalies between angular and classical means are shown in Fig. 12, we notice that there is a northward shift of tropical rainfall, which is the most manifested in JJA, reflecting the warming over Northern Hemisphere as in Fig. 9. The Sahal region experienced more "computed" precipitation in boreal summer, this is again consistent with the computed cooling there as depicted in Fig. 9. After calendar conversion, boreal autumn has the most pronounced changes, as shown in Fig. 13. The precipitation anomalies between 6k and 0k over Asia and Northern Africa is enlarged in SON with a magnitude of up to 0.5 mm/day.

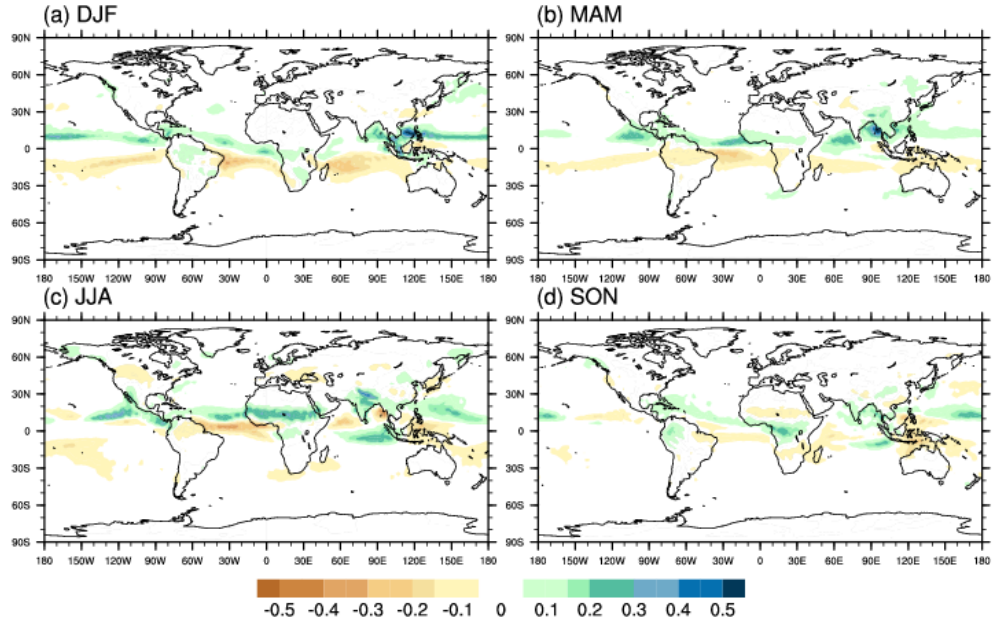

Figure 12: Mid-Holocene precipitation anomalies (mm/day) between angular and classical means performed by AWI-ESM1 (a) DJF, (b) MAM, (c) JJA, and (d) SON.

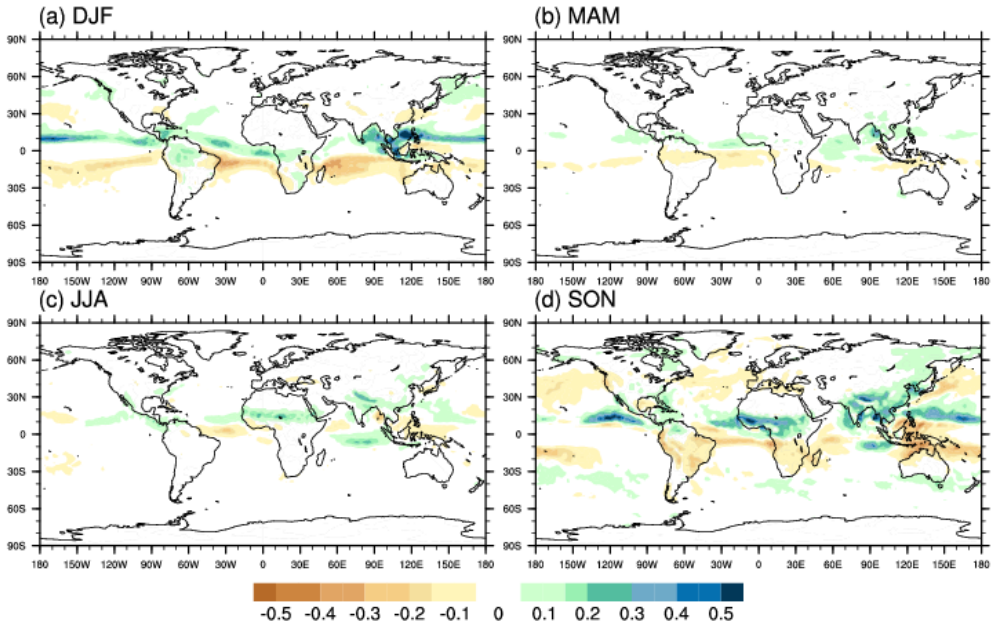

Figure 13: Differences in precipitation anomalies (6k-0k) between angular and classical means performed by AWI-ESM1 for (a) DJF, (b) MAM, (c) JJA, and (d) SON.

3.2.2 Last Interglacial

In the case of the LIG simulation, boreal summer insolation was even greater than the mid-Holocene (Fig. 12) and that forced eventually higher-than-present sea levels. Higher temperatures in the polar regions, particularly during the summer months, directly influence sea ice and the ice sheets. However in our simulation, we kept the sea level in 127k the same as present-day according to PMIP4 criteria, and we used fixed ice sheet configuration.

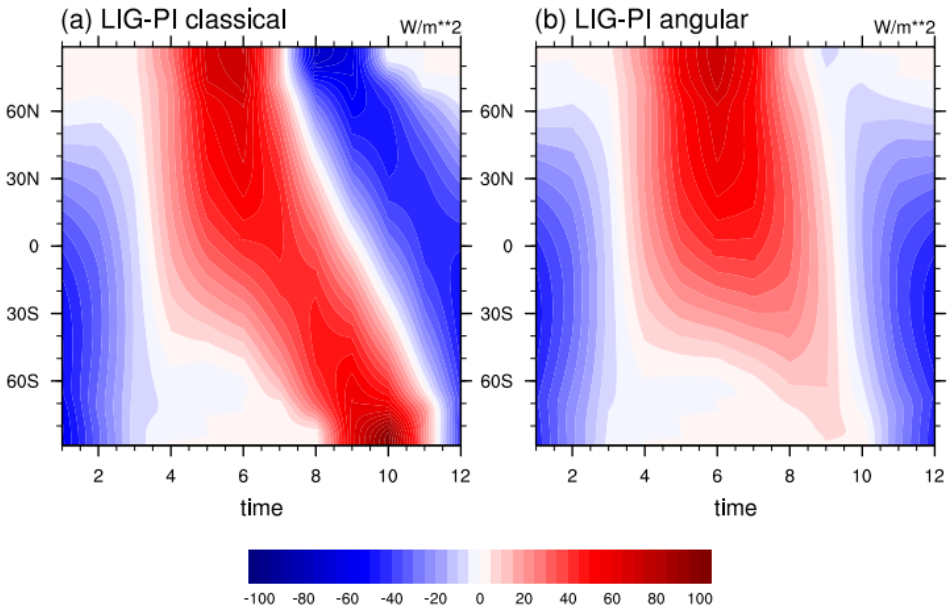

Figure 14: Difference of top-of-atmosphere insolation between 127k and 0k performed by AWI-ESM1 for (a) classical calendar and (b) angular calendar.

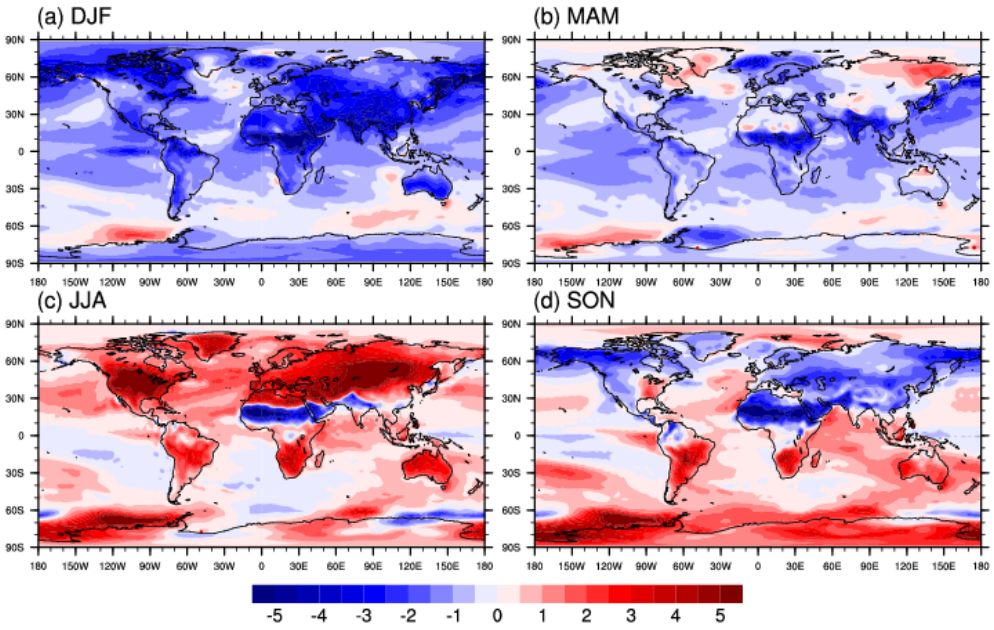

Figure 15: Difference of surface temperature between 127k and 0k performed by AWI-ESM1 under classical calendar.

Fig. 14 describes the insolation anomalies between the LIG and PI under classical fixed-day calendar (Fig. 14a) and angular (i.e., fixed-angle) calendar (Fig. 14b). Under the classical fixed-day calendar, the Northern Hemisphere high-latitudes experienced an increased solar insolation (up to 70 W/m2) from March to July as compared to PI, as well as a strong decrease (up to -70 W/m2) from August to October. For Southern Hemisphere, the maximum change in insolation happen in October over the south pole (over 90 W/m2). In winter months (December to February) the LIG-minus-PI insolation is negative (up to -50 W/m2).

While under angular calendar, the pattern is totally different: we observe a positive anomaly in incoming insolation for Northern Hemisphere from March to August. Throughout September to February, no significant difference can be seen for regions north of 60N, but we notice a negative anomaly in insolation in these months for 90S-60N. Over the Southern Hemisphere mid-to-high latitudes, only slight positive anomalies occur in September.

Due to the insolation changes between 127k and 0k (Fig. 14a), the simulated surface temperature in 127k shows an enhanced seasonality compared to present-day (Fig. 15) under classical calendar, which is much more pronounced than the mid-Holocene. In detail, DJF cooling of up to 5 K and JJA warming of more than 5 K are found for the Last Interglacial with regards to pre-industrial, especially over the Northern Hemisphere continents. Fig. 15 also illustrates a general cooling of LIG in MAM globally except some subpolar regions, but with much less pronounced pattern as compared to DJF. In boreal autumn, cooling in LIG in relative to PI occurs over Northern Hemisphere continents, while warming happens over Southern Hemisphere. We find cooling over Sahal region for all seasons, which reflect the increased clouds, rainfall and vegetation in the LIG than the present day.

Fig. 16 depicts the surface air temperature anomalies between LIG and PI but for angular calendar. The patterns for boreal winter, spring and summer is very similar to those shown by Fig. 15a-c. As mentioned above, during SON, we observe a general cooling/warming over the Northern/Southern Hemisphere under classical fixed-day calendar. The interesting thing is, such pattern over Northern Hemisphere in SON, however, flips its sign after conversion of calendar (Fig. 16), as we obtain a pronounced warming in LIG as compared to PI over Northern Hemisphere in SON under angular calendar.

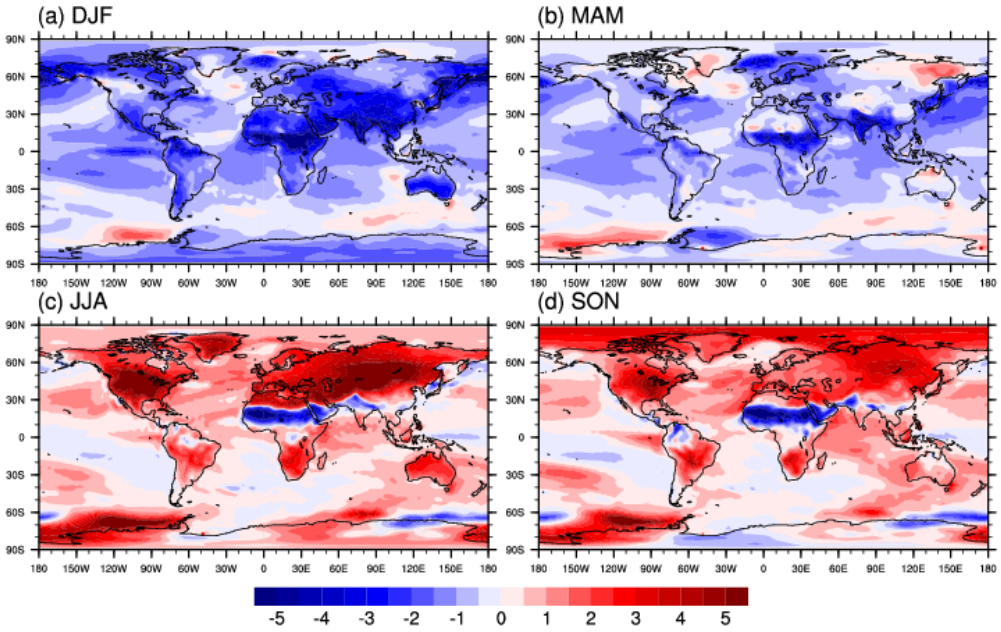

Figure 16: Difference of surface temperature between 127k and 0k performed by AWI-ESM1 under angular calendar.

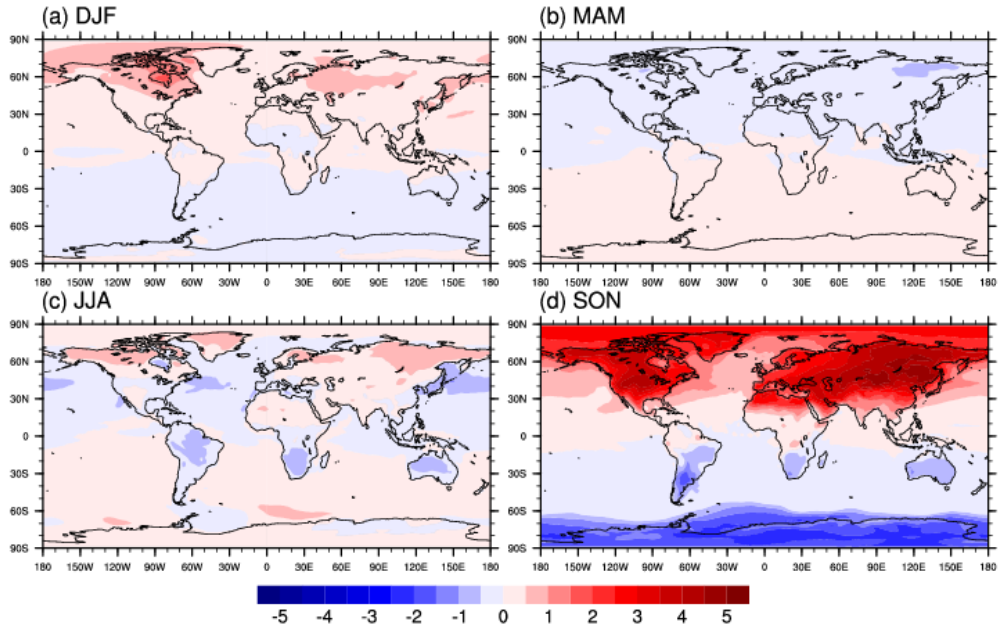

Figure 17: Differences in surface temperature anomalies (127k-0k) between angular and classical means performed by AWI-ESM1 for (a) DJF, (b) MAM, (c) JJA, and (d) SON.

As depicted in Fig. 17, the classical calendar tend to largely underestimate the warming of SON temperature anomalies over the Northern Hemisphere, such bias can be as large as 5 K. It also underestimate the anomalous cooling over the Antarctic. For other seasons, the calendar-caused bias is within a magnitude of 2 K. In DJF, cooling and warming bias can be found for the Northern and Southern Hemisphere under classical calendar respectively, while the opposite case is for the MAM. During boreal summer, the Northern Hemisphere oceans have a warming bias, while over other regions there is a general cooling bias under classical calendar.

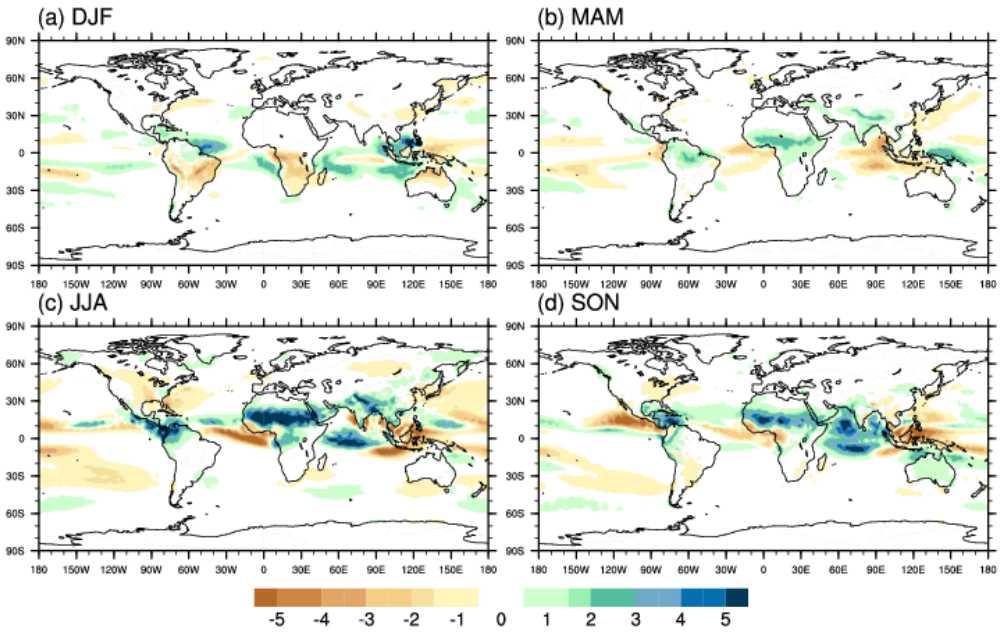

Figure 18: Difference of precipitation between 127k and 0k performed by AWI-ESM1 under classical calendar.

Fig. 18 shows the precipitation anomalies between Last Inter-glacial and pre-industrial. The pattern resembles that of the mid-Holocene, only larger in magnitudes. We notice a northward shift of the ITCZ, as there is a general wetter/drier condition to the north/south of the tropical rain belt.

Increase in precipitation is very significant over the Northern Africa in JJA and SON, indicating a stronger African summer monsoon in Last Inter-glacial compared to Pre-industrial.

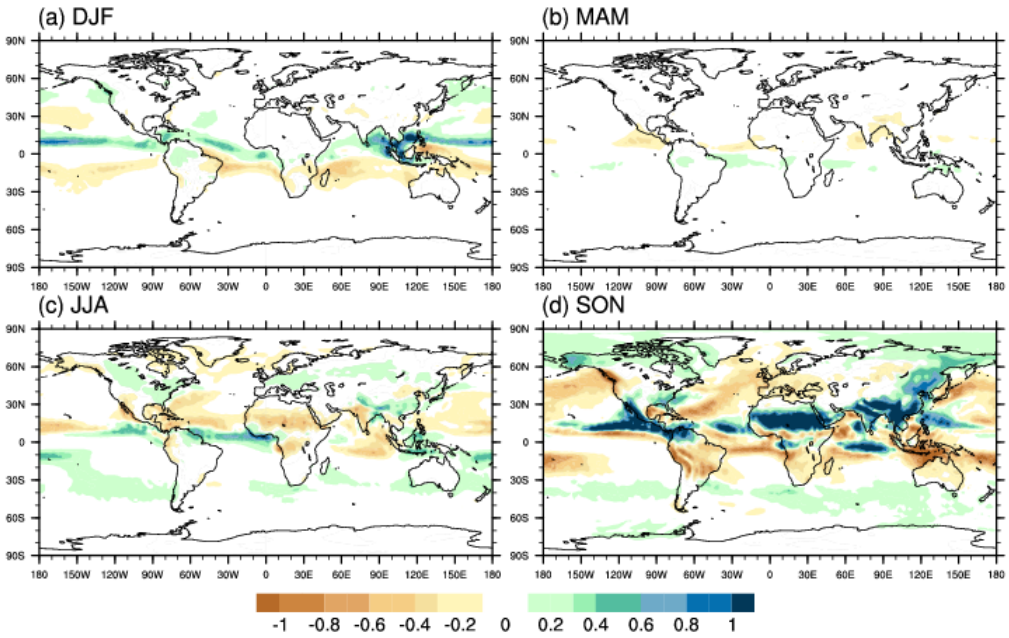

Figure 19: Differences in precipitation anomalies (127k-0k) between angular and classical means performed by AWI-ESM1 for (a) DJF, (b) MAM, (c) JJA, and (d) SON.

After we applied angular calendar to both 127k and 0k precipitation fields, we found less pronounced wetter condition in JJA and more significant increase in rainfall over Northern Africa (Fig. 19). This means that the classical calendar overestimate and underestimate the African summer monsoon precipitation for JJA and SON respectively.

3.2.3 Transient experiment

In this section we present results from a 6000-year transient simulation from 6k to 1950 CE. The transient experiment was conducted using AWI-ESM2. We applied the boundary conditions of the past 6,000 years. Orbital parameters are calculated according to Berger (1978), the greenhouse gases are taken from ice-core records and from recent measurements of firn air and atmospheric samples (Köhler et al., 2017). For more information we refer to Vorrath et al. (2020) and Carré et al. (2021). We firstly calculate for each year the shift of the starting date of each month in angular calendar as compared to classical fixed-day calendar which is shown in Fig. 20. Note here the shift of the starting date of one month can also stand for the shift of the end date of its previous month.

As seen from Fig. 20, January and February are delayed in fixed-angle as compared

to the fixed-length calendar, and the number of days delayed reduces with time. For March, there are a -1 day shift happening around 5 ka, and a 1 day shift after 1 ka. Since the VE is fixed at March 21, there are no shift of days for the beginning of April. May and June have generally a 1-day shift but for some time interval the shift is 2 days. July have a delay of 2-3 day in angular as compared to classical calendar. The delay for August (1-3 days) and September (0-3 days) generally increases with time. The last 3 months, i.e., October, November and December, is more advanced in angular calendar at 6 ka, but delayed at 0 ka.

Here we turn to investigate the evolution of temperature and precipitation in a transient simulation for the past 6,000 years, and the effect of calendar conversion on the time series of those two variables.

The transient experiment was conducted using AWI-ESM2. Here we present results for the region of the NH and the parameters considered are precipitation and temperature over land.

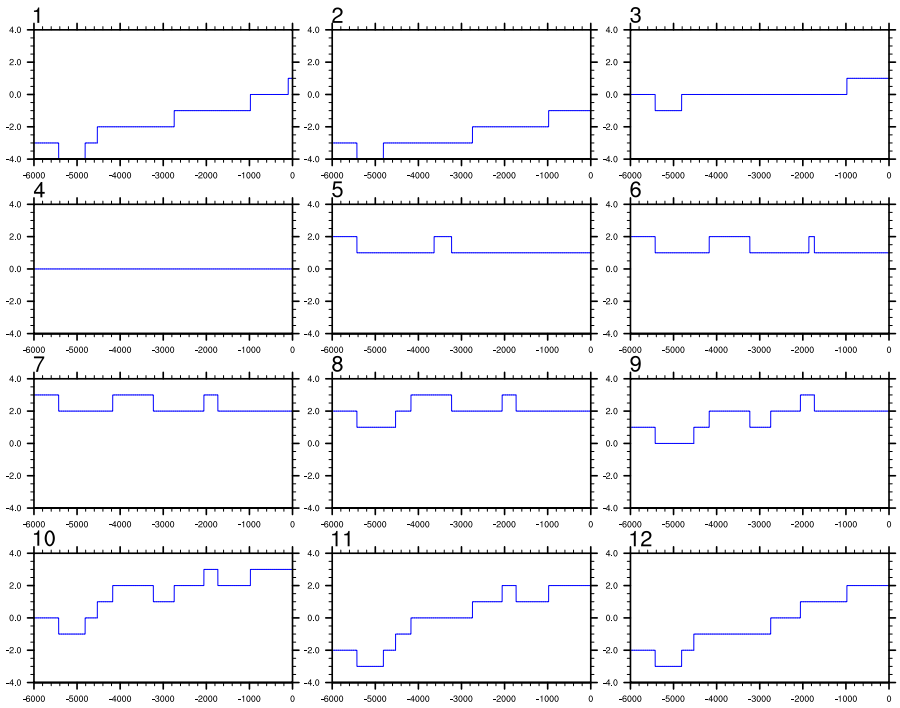

Figure 20: Shift of the first day for each month, from 6k to 0k. Units: day

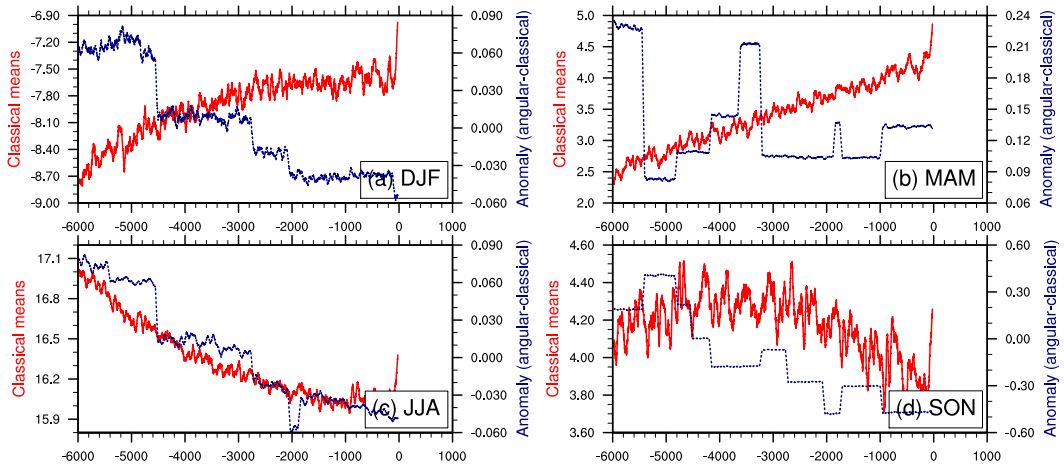

Figure 21: Temperature evolution over Northern Hemisphere land (red lines, axis to the left), and the anomaly (Angular-Classical means, blue lines, axis to the right), for (a) DJF, (b) MAM, (c) JJA, and (d) SON. Results are based on transient simulation by AWI-ESM2

Fig. 21 shows time series of mean Northern Hemisphere temperature over land for all seasons. In DJF, mean NH continental temperature tends to gradually increase from 6k to 0k, consistent with the increased NH solar insolation from 6k to 0k. The change of temperature after application of angular calendar is less than 0.1 K from 6k to 3k for DJF, and such bias generally reduces from 6k to 0k, accompanied by several fluctuations, which can be related to the changes in shift of boreal-winter days between the two calendars (see Fig. 20 for December and April). After 3k, we find a warming bias under classical calendar, which increases over time, and the bias magnitude is less than 0.06 K in pre-industrial.

Similar to DJF, MAM shows a gradual increase in Northern Hemisphere continental temperature from mid-Holocene to present. The calendar effect is the most manifested in 6-5.4k, with a cooling bias of 0.23 K in classical calendar. Most of the bias is suddenly removed since 5.4k with the adjusted-minus-unadjusted values being

less than 0.1 K. From 5.4 to 3.2k, the calculated temperature difference gradually increase to 0.2 K in angular as compared to classical calendar. Then the cooling bias maintains around 0.1 K from 3.2 k to present. From Fig. 21b, we observe fluctuations in the evolution of temperature differences from 6k to 0k. They are indeed associated with the shift of starting date of March (see Fig. 203) and the end date of May (see Fig. 206). One example is the wax and wane around 1.8k, which is explained by the change of shift in the end date of May, as shown in Fig. 206. It seems that there is a lack of reason for the jump in temperature bias happening at 3.6k, as neither the shift in starting date of March nor that in the end date of May has a change during that time interval. However, we notice that at 3.6 k, the shift in the starting date of May changes from 1 to 2 days. This will also affect the mean MAM temperature, as our mean MAM temperature values are calculated based on monthly means rather than daily means, so the length of each season during boreal spring matters in this case.

JJA shows a gradual decline of temperature from 18.2 °C in the 6k to 17 °C in present-day. There is also a gradual decline from the 6k till present day in the anomalous temperature caused by calendar conversion. Note that the temperature bias in JJA is not strong, with a magnitude being less than 0.1 °C, this is due to the fact that the range (starting and ending dates) of the summer days in angular summer is similar as in our present-day calendar (Table 3).

SON reveals warming from 6k to 3k, followed by a cooling from 3k to 0k. The temperature anomaly shows a declining trend. We notice that the SON temperature bias is the strongest among all seasons due to the relatively large shift in autumn days. Moreover, the evolution of the calendar effect on NH temperature for SON is strongly shaped by the shift in the starting date of November (see Fig. 2011) Over the Ocean, the pattern is very similar as that on land, only with a smaller magnitude (see Fig. 22).

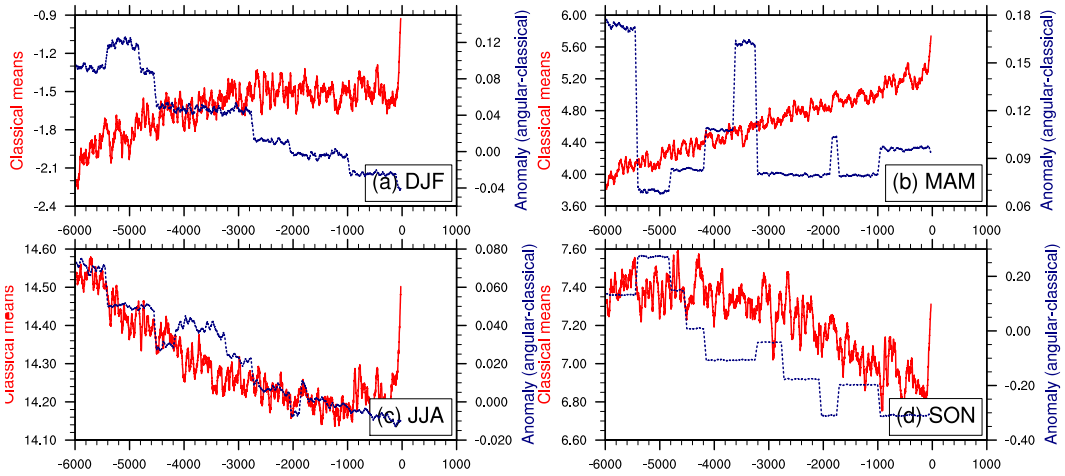

Figure 22: Temperature evolution over Northern Hemisphere oceans (red lines, axis to the left), and the anomaly (Angular-Classical means, blue lines, axis to the right), for (a) DJF, (b) MAM, (c) JJA, and (d) SON. Results are based on transient simulation by AWI-ESM2

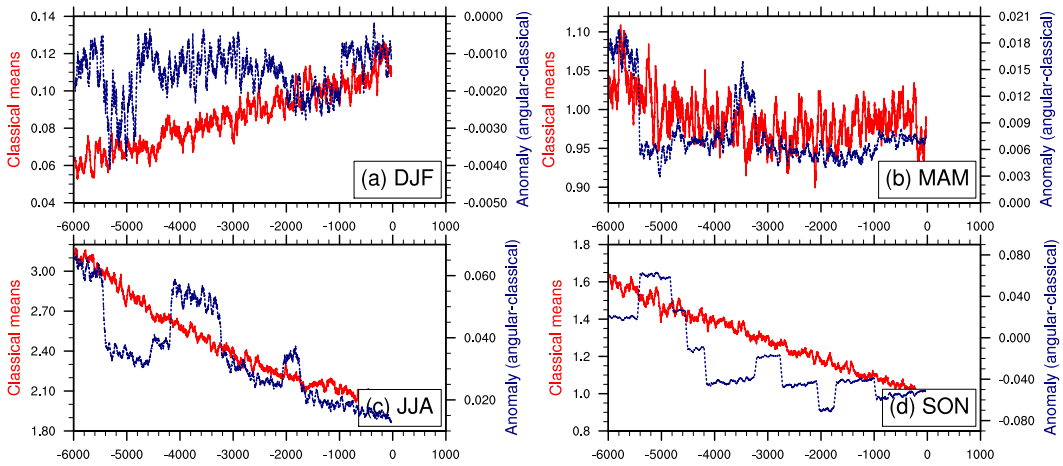

Figure 23: As in Fig. 21, but for precipitation over West Africa. Units: mm/day.

Our equilibrium simulation has shown that the most pronounced calendar effect on precipitation occurs over Africa monsoon domain. Here Fig. 23 shows the precipitation over West Africa for the period under investigation. For West Africa monsoon region we have chosen the domain of 0-30N; 15W-30E. Here we focus on the monsoon seasons, i.e., JJA and SON. As indicated in Fig. 23, the West Africa monsoon precipitation decreases from mid-Holocene to pre-industrial. As discussed in previous section, this is due to a northward shift of ITCZ in 6k as compared to present. The angular-minus classical precipitation averaged over the West Africa monsoon domain is less than 2% of the classical mean precipitation. Therefore the calendar effect, which weakens from 6k to present as seen in Fig. 23c,d, is not significant in this case. Researchers can decide whether they perform calendar correction when comparing 6k precipitation with present-day.

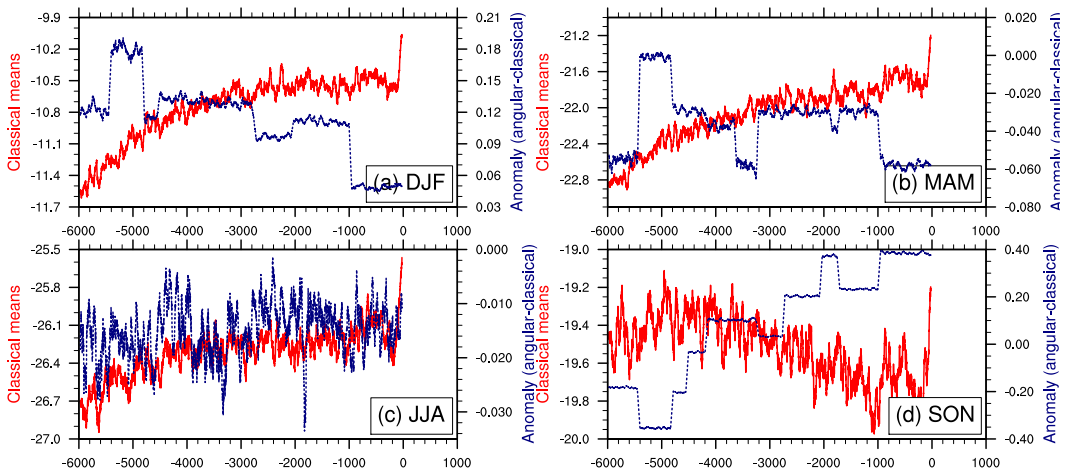

Figure 24: As in Fig. 21, but for mean surface temperature over Southern Hemisphere land. Units: °C

As seen in Fig. 24, over the SH, there appears to be a rising temperature over the SH continents from 6k till present in DJF, MAM and JJA but in SON, there was a

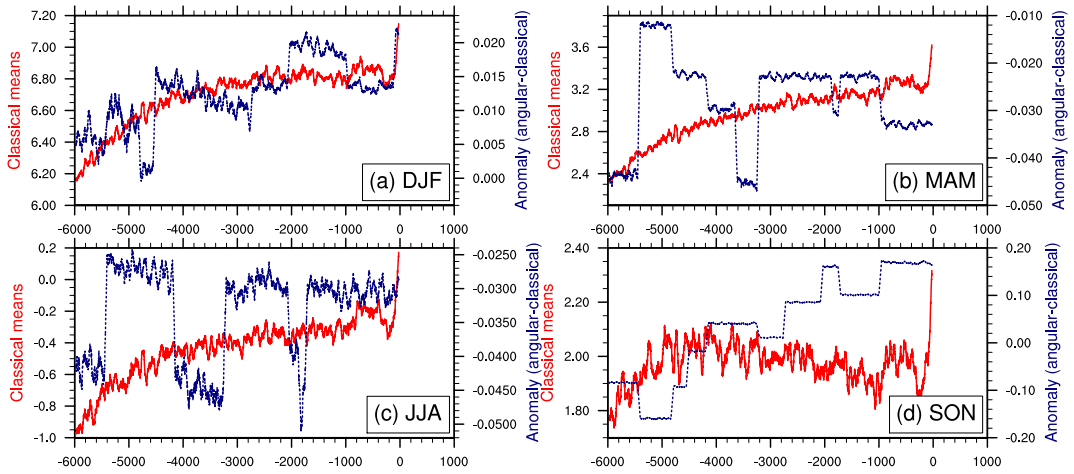

Figure 25: As in Fig. 21, but for mean surface temperature over Southern Hemisphere oceans. Units: °C

maintained stability around 4k, followed by a cooling to 0.1 k and then an abrupt warming during the last 100 years. The same signal could be found on ocean (Fig. 25). The calendar effect on SH temperature, similar to that of the NH, is the most pronounced in SON, however with the largest temperature difference occurring at present-day. The ocean pattern just mimics that of the land, only with smaller values. Here the detailed characteristic of the calendar effect on SH temperature will not be illustrated as their shapes are just the opposite to the NH counterpart.

3.3 Simulated El Nino and the Southern Oscillation

In this section we show the results about ENSO based on our transient simulation for the past 6,000 years. We put our focus on the Nino3.4 index and calculate its interannual variability and seasonality for the region of interest (i.e 5N-5S, 170W-120W). The inter-annual variability is calculated as the variance of annual value in 100-year sliding time-windows of Nino3.4 time series (of past 6,000 years) in which low frequency ($<$ 10 years) has been filtered out while the seasonality is calculated as the average annual range over a time period. In other words, we define the seasonality of Nino3.4 as the average amplitude of the annual cycle (maximum monthly SST - minimum monthly SST in a calendar year). A composite analysis is also done in order to get the response of climate to ENSO through time. In addition ENSO effect on monsoon precipitation in different time interval (6K to 0K) has been examined regionally and globally. For more detailed information we refer to section 2 of the present thesis.

3.3.1 Variability

Understanding ENSO variability is of great importance. This is because of its effects on precipitation which has significant teleconnections all around the globe. Reduced ENSO variability evident in proxy records during the mid-Holocene has indicated that this reduction is propelled by high boreal summer insolation and a stronger monsoon system Braconnot et al. (2012); Liu et al. (2000); Zhang et al. (2008). To test this trend, we use our model to run for 100 simulated time series and the subsequent result is seen in Fig. 26:

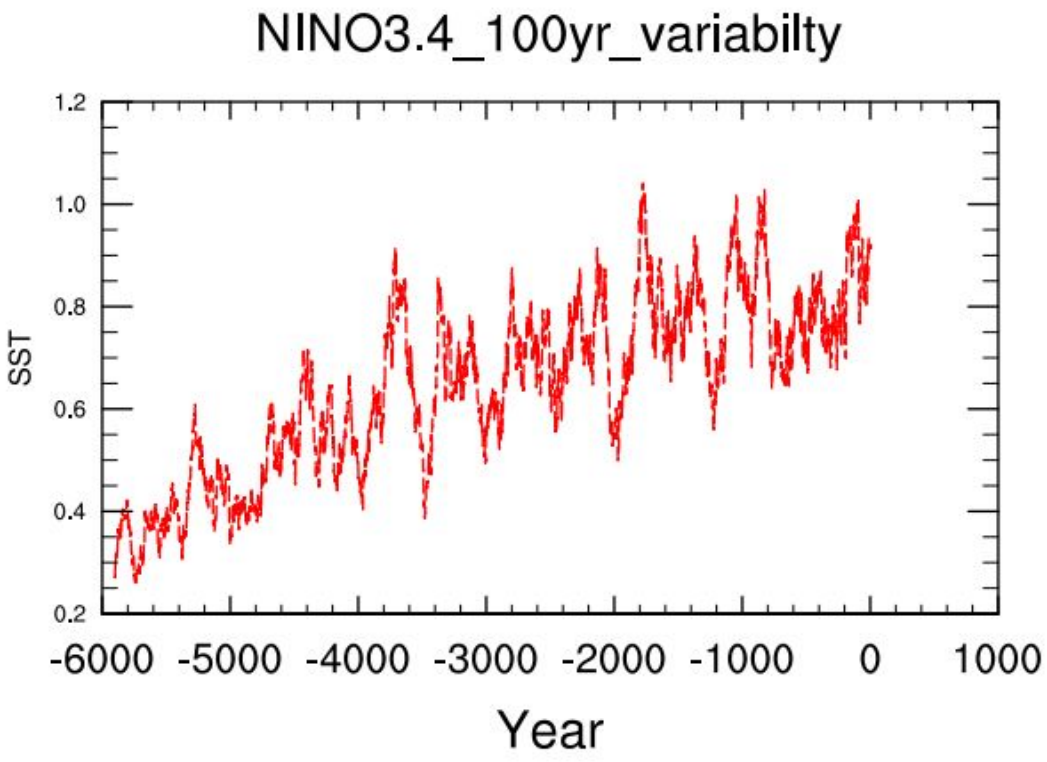

Figure 26: ENSO variablity for 100 simulated time series.

The figure shows a gradual increase over the time period. Which indicates that over the past 6,000 years, inter-annual variability has been increasing. The simulations shows an increasing trends of inter-annual variability from mid-Holocene to the present with a reduction in the ENSO variablity in the mid-Holocene. There is lower variability seen at 6k with a gradual,constant and steady increase as it approach 0k. But the pattern of low variability during the mid-Holocene, increasing after 3K suggesting that increasing variability is driven by the occurrence of extreme dry events, highlighting a strengthened El Niño phase.

Grothe et al. (2020) established that ENSO variability over the last five decades is approximately 25% stronger than during the pre-industrial which we can relate to in this study.

3.3.2 Seasonality

One of the key characteristics of ENSO is its synchronization to the annual cycle, which manifests in the tendency of ENSO events to peak during boreal winter (Stein et al., 2014) which has far-reaching impacts across the globe and it is becoming more

and more apparent that the regional impacts of ENSO tele-connections are highly sensitive to the seasonal evolution of ENSO events.

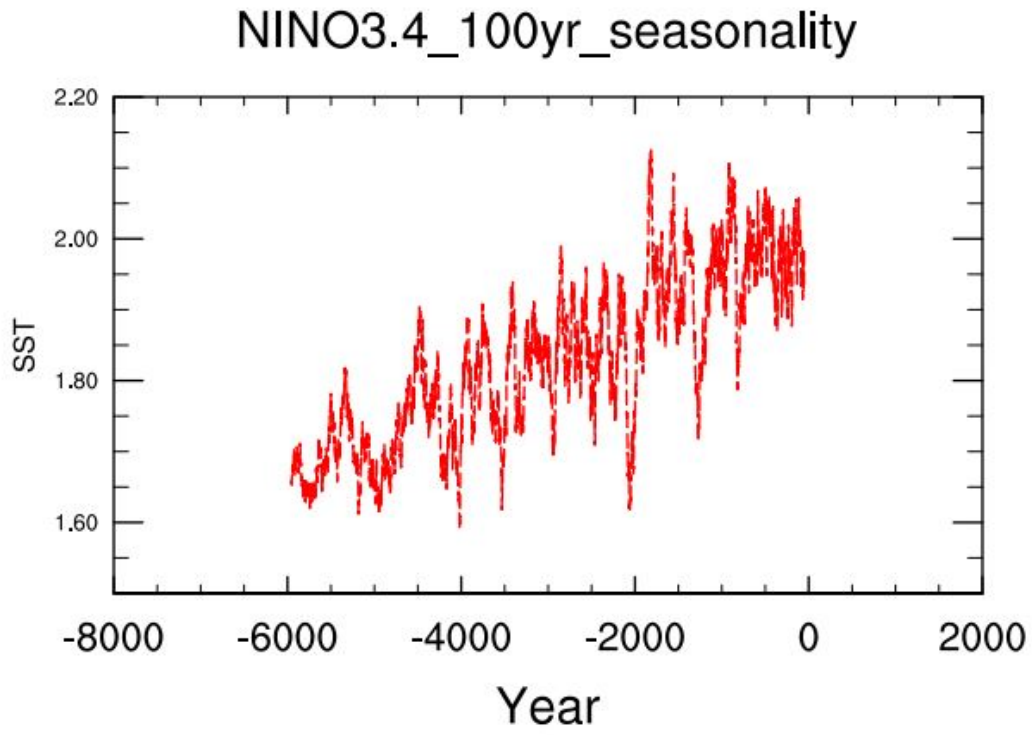

Figure 27: ENSO Seasonality for 100 simulated time series.

The result from the simulated seasonality shows an increases from mid-Holocene to the present. From the plot, there is a slight peak around 2K before maintaining a steady increase to 0K.

A typical ENSO event develops in the late boreal spring, peaks at the end of the calendar year (denoted as El Niño or La Niña), and decays in the following spring to early summer. However, the changes in seasonality can be as a result of reduction in ENSO magnitude which involves wave propagation along the thermocline, and the timing of the development of ENSO anomalies (Luan et al., 2012)

3.3.3 ENSO effect on Monsoon Precipitation

The summer monsoon precipitation is defined as rainfall received during the summer monsoon season (June, July and August). El Nino and Southern Oscillation

(ENSO) has been known to exert the most important external forcing on the monsoon region, bringing about deficit/excess of rainfall by shrinking/amplifying the convection over the region.

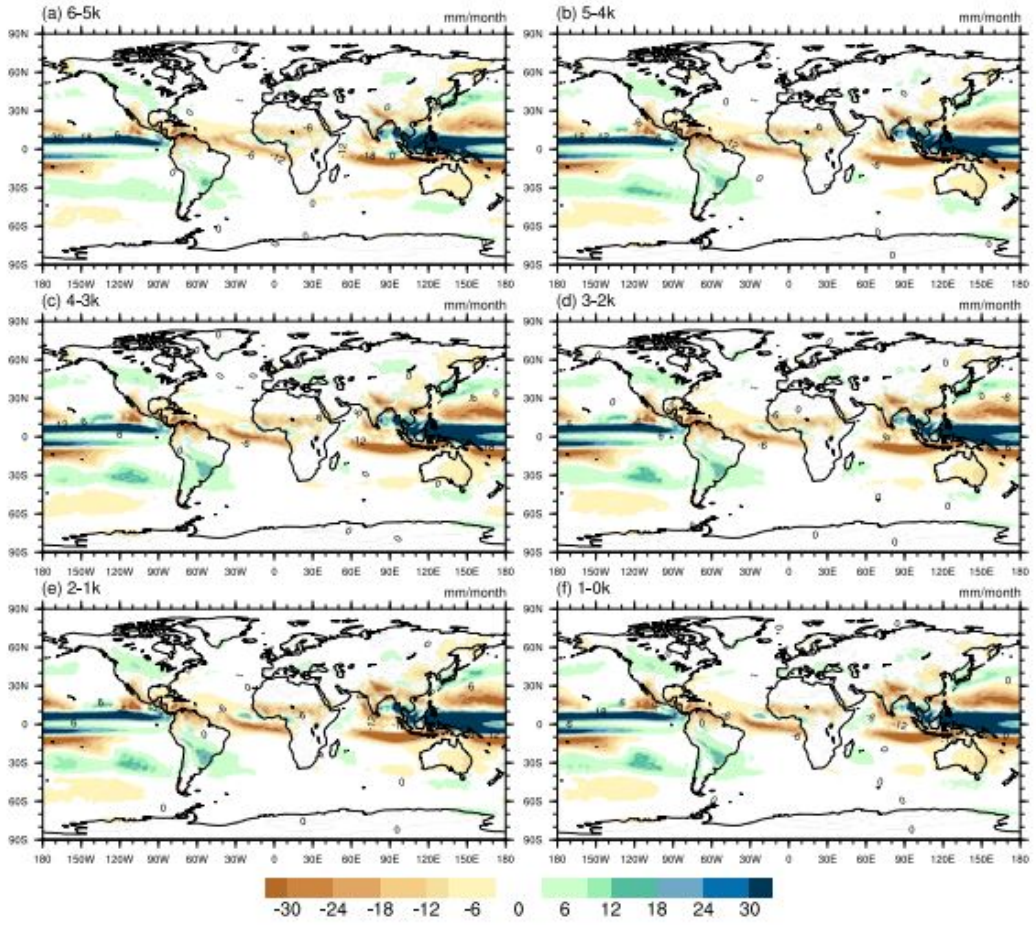

Figure 28: JJA ENSO effect on monsoon precipitation globally during different time intervals of the past 6,000 years.

As seen in Fig. 28, most of the changes or effect can be felt mostly in the equatorial regions for the time series under investigation. To better understand these effect, we will be focusing on 4 geographic regions of the equatorial pacific.

a. Africa

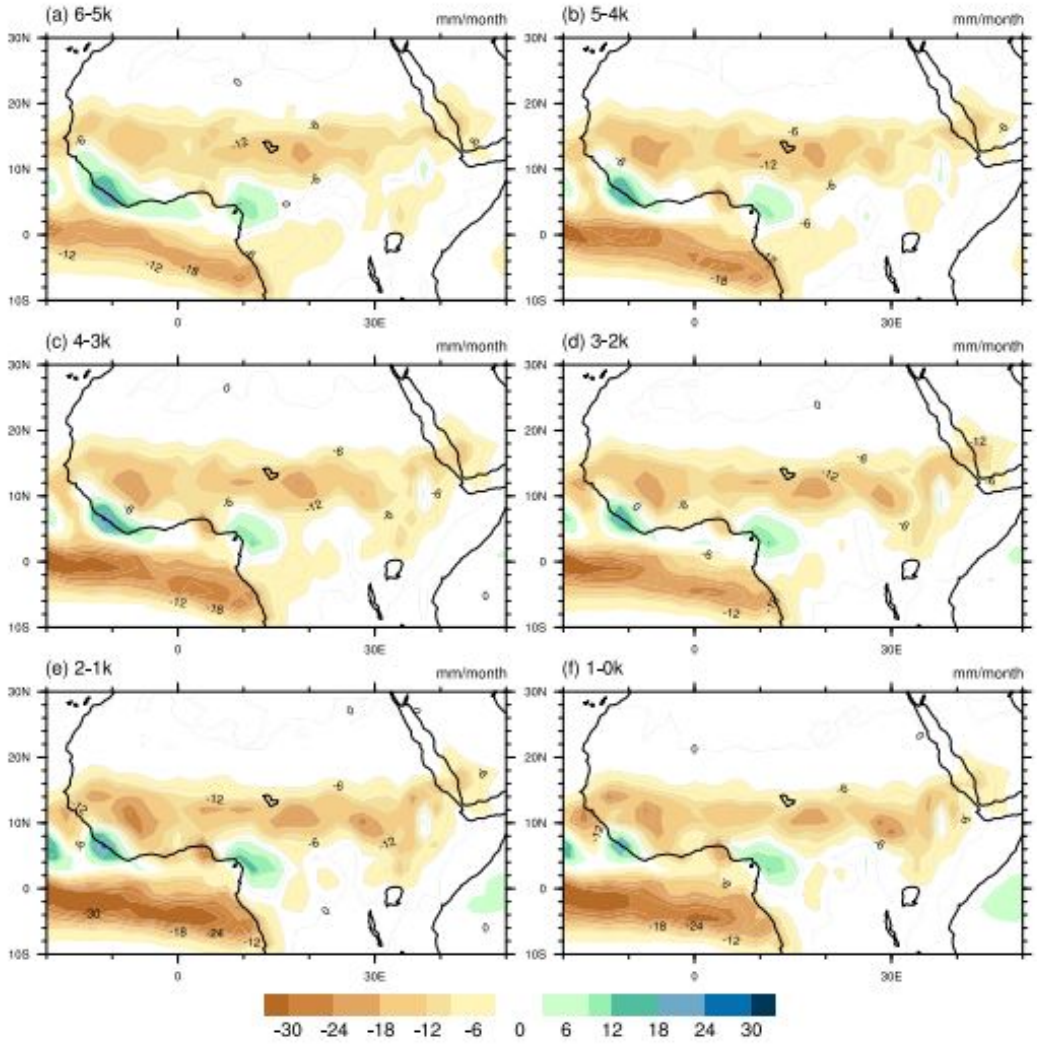

Figure 29: ENSO effect on monsoon precipitation in Africa during different time intervals of the past 6,000 years.

b. India

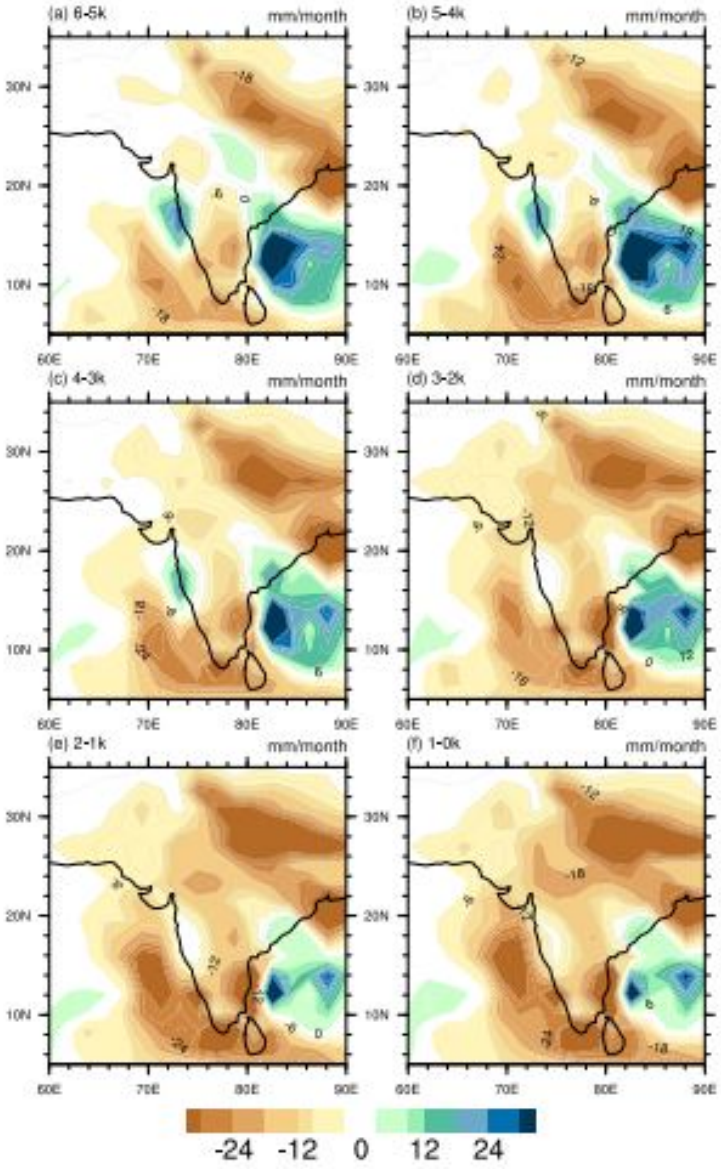

Figure 30: ENSO effect on monsoon precipitation in India during different time intervals of the past 6,000 years.

c. North America

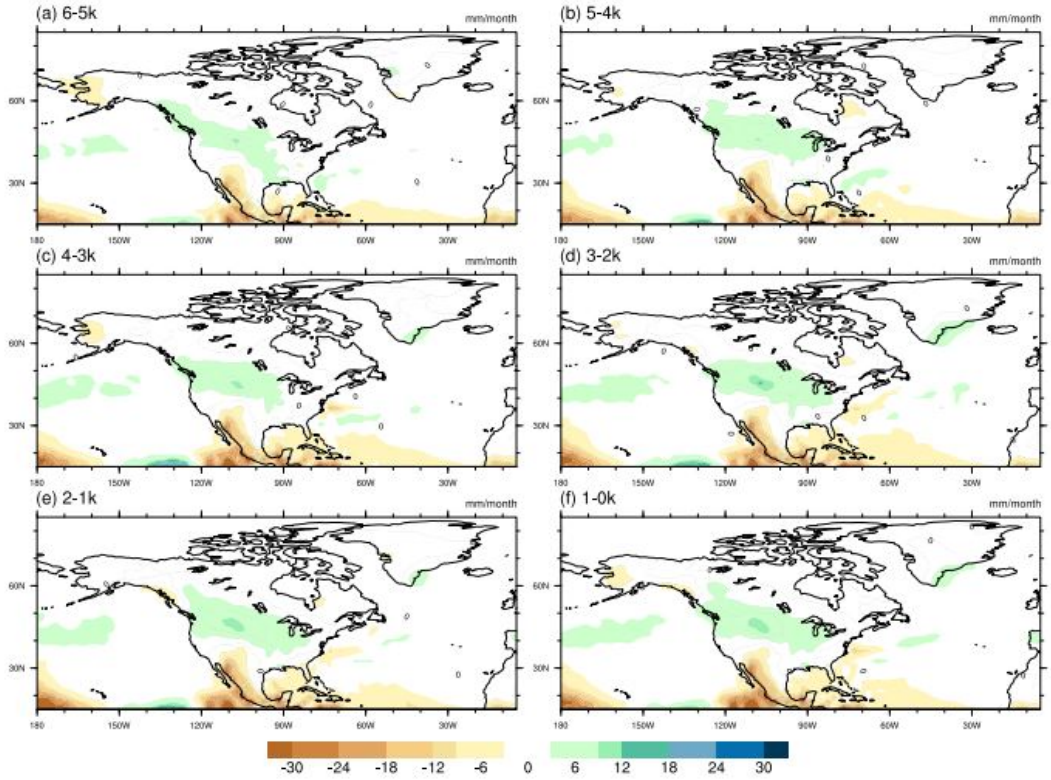

Figure 31: ENSO effect on monsoon precipitation in North America during different time intervals of the past 6,000 years.

d. South Asia

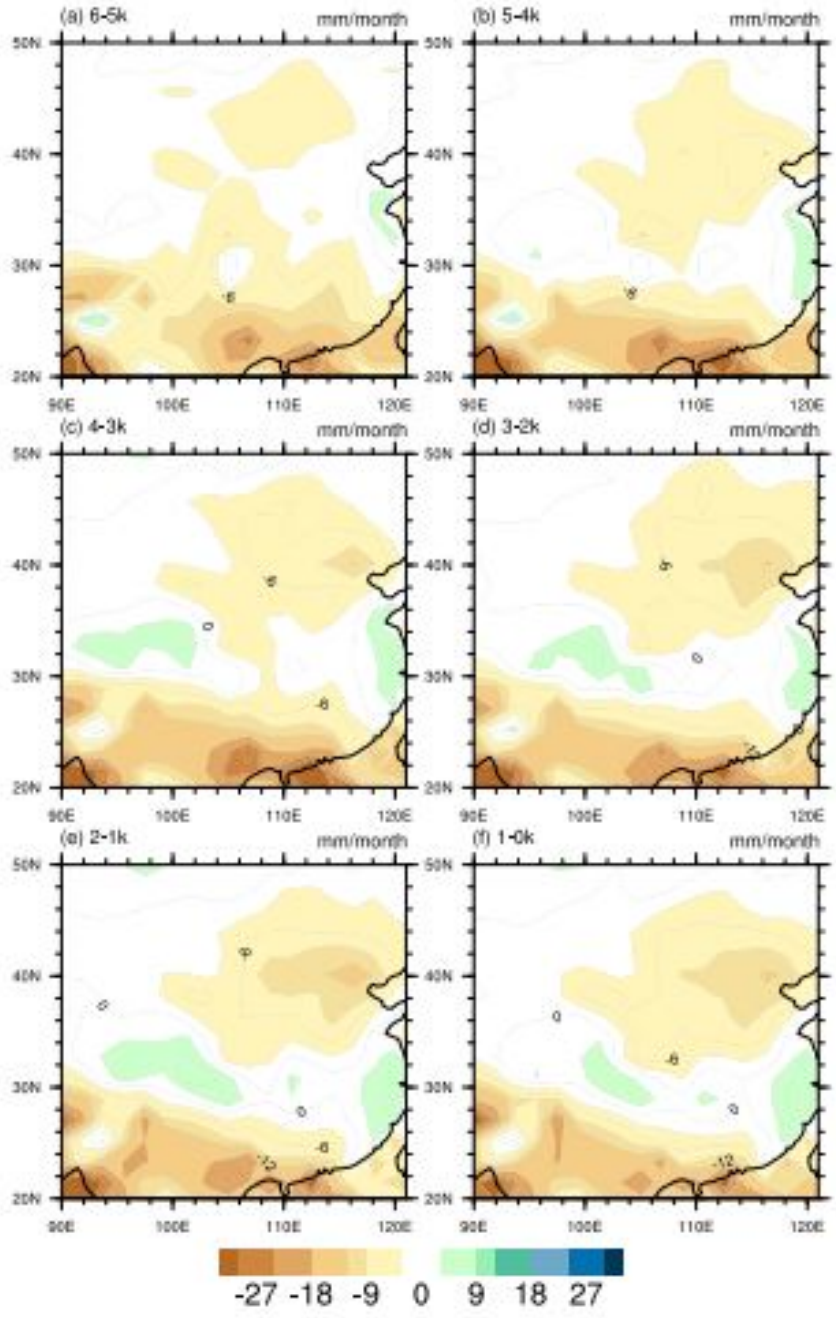

Figure 32: ENSO effect on monsoon precipitation in South Asia during different time intervals of the past 6,000 years.

In the Fig. 29 to Fig. 32, the attention is on the drying signal which shows no obvious change in the relationship. However on a closer observation, the magnitude of change through time is quite infinitesimal.

4 Conclusion and Discussion

The present study was carried out to investigate the response of seasonality definition on simulated seasonal cycle of surface air temperature and precipitation, putting into consideration MH and LIG with respect to PI.

The AWI-ESM1 and AWI-ESM2 used in this study is a high resolution coupled climate model providing enabling environment for simulating modern background climate. The AWI-ESM1 comprises of an atmosphere module ECHAM6 and an ice-ocean module FESOM1.4, while AWI-ESM2 shares with AWI-ESM1 the same atmosphere module while has a more advanced ocean component FESOM2.0. With respect to the boundary conditions and orbital configuration (Table 3) in the simulation for MH and LIG and PI, we have applied orbital parameters and greenhouse gases according to the standard criteria of PMIP4. Our simulations show a stronger seasonality in MH/LIG as compared to PI as a response to the change in insolation, and such change is more pronounced in LIG.

Taking surface temperature as a climate indicator, our simulations illustrate warming (cooling) in SON (DJF) over the Arctic, regions of the tropical and sub-tropical experience warming (cooling) in JJA (DJF) and over the Antarctic warming (Cooling) in JJA and SON (DJF and MAM) as analyzed in the MH. Fig. 16 reveals that LIG experienced more precipitation over Africa, North America and Asia. Rainfall was experienced more in MH but the Monsoon precipitation over NH was stronger because of the ITCZ shift (Fig. 8).

For MH climate, the angular calendar leads to a homogeneous warming over the Northern Hemisphere with regards to classical means, which finds its greatest expression over the continent in MAM with a temperature change of more than 0.5 K. However, for the anomalies between MH and PI, the most pronounced difference occurs in SON rather than in MAM between the angular and the classical methods. This can be explained by the fact that the present-day fixed-day calendar tend to overestimate the temperature of Northern Hemisphere in PI. In terms of LIG, the most intriguing feature is the large cooling bias in SON as calculated by the classical calender. This is mainly driven by the large shift and difference in the SON days defined by the two calendars, and the change in precession is responsible for the shift. In addition, fix-day calendar tend to underestimate the Africa summer monsoon precipitation in MH during both JJA and SON, while in LIG the fix-day

calendar leads to an overestimation/underestimation of the Africa summer monsoon rainfall in JJA and SON respectively.

Our results support the idea of that the choice of paleo calendar is important and a fix-day calendar applied in simulated paleo climate could lead to large bias in terms of both surface air temperature and precipitation. It might also affect the accuracy of the results from model-data comparison, as the reconstructured proxy records could be significantly affected by the seasonality of the past climate. Therefore, we call for a more careful interpretation in model-data comparison and the choice of seasonality definition in simulated paleo climate.

Our method for calendar definition is similar as the one used in Bartlein and Shafer (2019), with however some differences: In the work of Bartlein and Shafer (2019), the pure effect of calendar has been investigated, this was achieved by performing 6k and 127k calendar conversion based on modern state; whilst in our study, the conversion was conducted for the respective time period. Another difference lies on the treatment of modern calendar. Bartlein and Shafer (2019) did not correct the seasonality for modern climate, which has been considered in the present study as the modern fixed-day calendar is a non-angular calendar and therefore needs to be converted as well.

In addition to the equilibrium simulations, we also performed a transient simulation for the past 6,000 years with daily outputs. We explored the calendar effect in this transient simulation in terms of the averaged surface temperature over Northern Hemisphere continents, Northern Hemisphere oceans, Southern Hemisphere continents, and Southern Hemisphere oceans, as well the precipitation over the Africa summer monsoon domain. Our results from the transient simulation reveal a temporal-variable effect of calendar on both temperature and precipitation, which generally reduces with time.

The characteristics of ENSO in our transient simulation has been examined. We find an increased ENSO interannual variability and seasonality from 6k to 0k, which is in good agreement with a multi-model study by Carré et al. (2021). Results from a composite analysis between ENSO and precipitation indicate a drying effect of ENSO on the Northern Hemisphere monsoon rainfall, in particular over the Africa summer monsoon domain. Furthermore, we find such teleconnection between ENSO and the Africa summer monsoon precipitation weakens from 6k to present. However, the reason behind such phenomenon still need to be examined. The same pattern

can be found also for other Northern Hemisphere monsoon domains such as North America, Indian and Southeast Asia.

5 Outlook

In the present study we briefly introduced the calendar effect in both time-slice and transient simulations, with a focus on the surface temperature and precipitation. In the following step, we will try to look at other important elements such as sea ice. Furthermore, we would like to derive the calendar effect on the seasonal insolation in our transient simulation, to see if the insolation bias caused by the classical calendar lineally changes with time. It is also interesting to investigate if the calendar effect can be magnified by large-scale climate patterns like the El Nino and the Southern Oscillation (ENSO) and the Atlantic meridional overturning circulation (AMOC). Also, we would like to further focus on more local regions, such as North America, South Asia and Indian, to examine the calendar effect in a more regional view. As more model outputs are available, we would like to compare our results with other model members such as those from PMIP4 (equilibrium simulations) and PACMEDY (transient simulations).

Acronyms

AWI Alfred Wegener Institute.

AWI-ESM Alfred Wegener Institute-Earth System Model.

AWI-ESM1 Alfred Wegener Institute-Earth System Model 1.

AWI-ESM2 Alfred Wegener Institute-Earth System Model 2.

CCSM3 Community Climate System Model version 3.

CDO Climate Data Operator.

CMIP Coupled Model Inter-Comparison Project.

CPU Central Processing Unit.

CSM Climate System Model.

DJF December-January-February.

DKRZ The German Climate Computing Center.

EC European Center.

ECHAM European Center-Hamburg Model.

ECHAM6 European Center-Hamburg Model, Version 6.

ECMWF European Center for Medium Range Weather Forecasts.

ENSO El Nino and the Southern Oscillation.

ESOI Equatorial Southern Oscillation Index.

FESOM Finite Element Sea-ice Ocean Circulation Model.

GRIB General Regularly-Distributed Information in Binary form.

HLRE-3 High Performance Computing System for Earth System Research -3.

HPEs Hydrostatic Primitive Equations.

ITCZ Inter-Tropical Convergence Zone.

JJA June-July-August.

LGM Last Glacial Maximum.

LIG Last-Inter-Glacial.

MAM March-April-May.

MH Mid-Holocene.

MPI Max-Planck-Institute.

MRM onth running mean.

NCAR National Center for Atmospheric Research.

NCL NCAR Command Language.

NetCDF Network Common Data Form.

NH Northern Hemisphere.

NOAA National Oceanic and Atmospheric Administration.

OLR Outgoing Long-wave Radiation.

ONI Oceanic Nino Index.

PI Pre-Industrial.

PMIP Paleoclimate Modeling Intercomparison Project.

PMIP4 Paleoclimate Modelling Intercomparison Project 4.

SH Southern Hemisphere.

SLP Sea Level Presure.

SOI Southern Oscillation Index.

SON September-October-November.

SST Sea Surface Temperatures.

UCAR University Corporation for Atmospheric Research.

VE Vernal Equinox.

References

Allan, R., Lindesay, J., Parker, D., et al. (1996). *El Niño southern oscillation & climatic variability*. CSIRO publishing.

An, S.-I. and Wang, B. (2000). Interdecadal change of the structure of the enso mode and its impact on the enso frequency. *Journal of Climate*, 13(12):2044–2055.

Barnston, A. (2015). Why are there so many enso indexes, instead of just one. *NOAA Climate. gov*.

Bartlein, P. J. and Shafer, S. L. (2019). Paleo calendar-effect adjustments in time-slice and transient climate-model simulations (paleocaladjust v1. 0): impact and strategies for data analysis. *Geoscientific Model Development*, 12(9).

Berger, A. (1978). Long-term variations of daily insolation and quaternary climatic changes. *Journal of the atmospheric sciences*, 35(12):2362–2367.

Braconnot, P., Joussaume, S., De Noblet, N., and Ramstein, G. (2000). Mid-holocene and last glacial maximum african monsoon changes as simulated within the paleoclimate modelling intercomparison project. *Global and planetary change*, 26(1-3):51–66.

Braconnot, P., Luan, Y., Brewer, S., and Zheng, W. (2012). Impact of earth's orbit and freshwater fluxes on holocene climate mean seasonal cycle and enso characteristics. *Climate dynamics*, 38(5-6):1081–1092.

Brierley, C., Zhao, A., and Harrison, S. P. e. a. (2020). Large-scale features and evaluation of the pmip4-cmip6 midholocene simulations. *Climate of the Past*, 16:1847–1872.

Brown, J. R., Brierley, C. M., An, S.-I., Guarino, M. V., Stevenson, S., Williams, C. J., Zhang, Q., Zhao, A., Braconnot, P., Brady, E. C., et al. (2020). Comparison of past and future simulations of enso in cmip5/pmip3 and cmip6/pmip4 models. *Climate of the Past*, 16:1777–1805.

Carré, M., Braconnot, P., Elliot, M., d'Agostino, R., Schurer, A., Shi, X., Marti, O., Lohmann, G., Jungclaus, J., Cheddadi, R., et al. (2021). High-resolution marine data and transient simulations support orbital forcing of enso amplitude since the mid-holocene. *Quaternary Science Reviews*, 268:107125.

Chiodi, A. M. and Harrison, D. E. (2013). El niño impacts on seasonal us atmospheric circulation, temperature, and precipitation anomalies: The olr-event perspective. *Journal of Climate*, 26(3):822–837.

Clement, A. C., Seager, R., and Cane, M. A. (2000). Suppression of el niño during the mid-holocene by changes in the earth's orbit. *Paleoceanography*, 15(6):731–737.

Cole, J. (2001). A slow dance for el niño. *Science*, 291(5508):1496–1497.

Dahlman, L. (2016). Climate variability: Oceanic niño index.

Danabasoglu, G., Yeager, S. G., Bailey, D., Behrens, E., Bentsen, M., Bi, D., Biastoch, A., Böning, C., Bozec, A., Canuto, V. M., et al. (2014). North atlantic simulations in coordinated ocean-ice reference experiments phase ii (core-ii). part i: mean states. *Ocean Modelling*, 73:76–107.

Danby, J. and Burkardt, T. (1983). The solution of kepler's equation, i. *Celestial Mechanics*, 31(2):95–107.

Danilov, S., Sidorenko, D., Wang, Q., and Jung, T. (2017). The finite-volume sea ice–ocean model (fesom2). *Geosci. Model Dev.*, 10:765–789.

Gagan, M. K., Ayliffe, L. K., Hopley, D., Cali, J. A., Mortimer, G. E., Chappell, J., McCulloch, M. T., and Head, M. J. (1998). Temperature and surface-ocean water balance of the mid-holocene tropical western pacific. *Science*, 279(5353):1014–1018.

Gergis, J. L. and Fowler, A. M. (2009). A history of enso events since ad 1525: implications for future climate change. *Climatic Change*, 92(3):343–387.

Glantz, M., Katz, R., and Nicholls, N. (1991). *Teleconnections linking worldwide climate anomalies*. Cambridge University Press.

Glantz, M. H., Glantz, M. H., et al. (2001). *Currents of change: impacts of El Niño and La Niña on climate and society*. Cambridge University Press.

Grothe, P. R., Cobb, K. M., Liguori, G., Di Lorenzo, E., Capotondi, A., Lu, Y., Cheng, H., Edwards, R. L., Southon, J. R., Santos, G. M., et al. (2020). Enhanced el niño–southern oscillation variability in recent decades. *Geophysical Research Letters*, 47(7):e2019GL083906.

Gu, D. and Philander, S. (1995). Secular changes of annual and interannual variability in the tropics during the past century. *Journal of Climate*, 8(4):864–876.

Iacono, M. J., Delamere, J. S., Mlawer, E. J., Shephard, M. W., Clough, S. A., and Collins, W. D. (2008). Radiative forcing by long-lived greenhouse gases: Calculations with the aer radiative transfer models. *Journal of Geophysical Research: Atmospheres*, 113(D13).

Joly, M. and Voldoire, A. (2009). Influence of enso on the west african monsoon: temporal aspects and atmospheric processes. *Journal of Climate*, 22(12):3193–3210.

Joussaume, S. and Braconnot, P. (1997). Sensitivity of paleoclimate simulation results to season definitions. *Journal of Geophysical Research: Atmospheres*, 102(D2):1943–1956.

Joussaume, S. and Taylor, K. (1995). Status of the paleoclimate modeling intercomparison project (pmip). *World Meteorological Organization-Publications-WMO TD*, pages 425–430.

Joussaume, S., Taylor, K., Braconnot, P., Mitchell, J., Kutzbach, J., Harrison, S., Prentice, I., Broccoli, A., Abe-Ouchi, A., Bartlein, P., et al. (1999). Monsoon changes for 6000 years ago: results of 18 simulations from the paleoclimate modeling intercomparison project (pmip). *Geophysical Research Letters*, 26(7):859–862.

Kageyama, M., Albani, S., Braconnot, P., Harrison, S. P., Hopcroft, P. O., Ivanovic, R. F., Lambert, F., Marti, O., Peltier, W. R., Peterschmitt, J. Y., et al. (2017). The pmip4 contribution to cmip6-part 4: Scientific objectives and experimental design of the pmip4-cmip6 last glacial maximum experiments and pmip4 sensitivity experiments. *Geoscientific Model Development*, 10(11):4035–4055.

Kageyama, M., Harrison, S. P., Kapsch, M.-L., Löfverström, M., Lora, J. M., Mikolajewicz, U., Sherriff-Tadano, S., Vadsaria, T., Abe-Ouchi, A., Bouttes, N., et al. (2020a). The pmip4-cmip6 last glacial maximum experiments: preliminary results and comparison with the pmip3-cmip5 simulations. *Climate of the Past*.

Kageyama, M., Sime, L. C., Sicard, M., Guarino, M. V., de Vernal, A., Schroeder, D., Stein, R., Malmierca Vallet, I., Abe-Ouchi, A., Bitz, C., et al. (2020b). A multi-model cmip6 study of arctic sea ice at 127ka: Sea ice data compilation and model differences. *Climate of the Past Discussions*.

Köhler, P., Nehrbass-Ahles, C., Schmitt, J., Stocker, T. F., and Fischer, H. (2017). A 156 kyr smoothed history of the atmospheric greenhouse gases co2, ch4, and n2o and their radiative forcing. *Earth System Science Data*, 9(1):363–387.

Kucharski, F., Bracco, A., Yoo, J., and Molteni, F. (2007). Low-frequency variability of the indian monsoon–enso relationship and the tropical atlantic: The "weakening" of the 1980s and 1990s. *Journal of Climate*, 20(16):4255–4266.

Kutzbach, J., Gallimore, R., Harrison, S., Behling, P., Selin, R., and Laarif, F. (1998). Climate and biome simulations for the past 21,000 years. *Quaternary Science Reviews*, 17(6-7):473–506.

Large, W. and Yeager, S. (2009). The global climatology of an interannually varying air–sea flux data set. *Climate dynamics*, 33(2-3):341–364.

Laskar, J. (1993). Frequency analysis of a dynamical system. *Celestial Mechanics and Dynamical Astronomy*, 56(1-2):191–196.

Lau, N.-C. and Nath, M. J. (1996). The role of the "atmospheric bridge" in linking tropical pacific enso events to extratropical sst anomalies. *Journal of Climate*, 9(9):2036–2057.

Lau, N.-C. and Nath, M. J. (2003). Atmosphere–ocean variations in the indo-pacific sector during enso episodes. *Journal of Climate*, 16(1):3–20.

Liu, Z., Kutzbach, J., and Wu, L. (2000). Modeling climate shift of el nino variability in the holocene. *Geophysical Research Letters*, 27(15):2265–2268.

Lohmann, G., Butzin, M., Eissner, N., Shi, X., and Stepanek, C. (2020). Abrupt climate and weather changes across time scales. *Paleoceanography and Paleoclimatology*, 35(9):e2019PA003782.

Lott, F. (1999). Alleviation of stationary biases in a gcm through a mountain drag parameterization scheme and a simple representation of mountain lift forces. *Monthly weather review*, 127(5):788–801.

Loveland, T. R., Reed, B. C., Brown, J. F., Ohlen, D. O., Zhu, Z., Yang, L., and Merchant, J. W. (2000). Development of a global land cover characteristics database and igbp discover from 1 km avhrr data. *International Journal of Remote Sensing*, 21(6-7):1303–1330.

Luan, Y., Braconnot, P., Yu, Y., Zheng, W., and Marti, O. (2012). Early and mid-holocene climate in the tropical pacific: Seasonal cycle and interannual variability induced by insolation changes. *Climate of the Past*, 8(3):1093–1108.

McGregor, H. V. and Gagan, M. K. (2004). Western pacific coral δ18o records of anomalous holocene variability in the el niño–southern oscillation. *Geophysical Research Letters*, 31(11).

McPhaden, M. J., Zebiak, S. E., and Glantz, M. H. (2006). Enso as an integrating concept in earth science. *science*, 314(5806):1740–1745.

Meehl, G., Gent, P., Arblaster, J., Otto-Bliesner, B., Brady, E., and Craig, A. (2001). Factors that affect the amplitude of el niño in global coupled climate models. *Climate Dynamics*, 17(7):515–526.

Milankovitch, M. (1941). History of radiation on the earth and its use for the problem of the ice ages. *K. Serb. Akad. Beogr.*

Otto-Bliesner, B., Brady, E., Zhao, A., Brierley, C., Axford, Y., Capron, E., Govin, A., Hoffman, J., Isaacs, E., Kageyama, M., et al. (2020). Large-scale features of last interglacial climate: Results from evaluating the lig127k simulations for cmip6-pmip4. *Climate of the Past Discussions*.

Otto-Bliesner, B. L. (1999). El nino/la nina and sahel precipitation during the middle holocene. *Geophysical Research Letters*, 26(1):87–90.

Otto-Bliesner, B. L., Brady, E. C., Clauzet, G., Tomas, R., Levis, S., and Kothavala, Z. (2006). Last glacial maximum and holocene climate in ccsm3. *Journal of Climate*, 19(11):2526–2544.

Otto-Bliesner, B. L., Brady, E. C., Shin, S.-I., Liu, Z., and Shields, C. (2003). Modeling el niño and its tropical teleconnections during the last glacial-interglacial cycle. *Geophysical Research Letters*, 30(23).

Pezet, F. (1895). The counter current "el niño," on the coast of northern peru. In *Report of the Sixth International Geographical Congress*, volume 6, pages 603–606.

Power, S., Haylock, M., Colman, R., and Wang, X. (2006). The predictability of interdecadal changes in enso activity and enso teleconnections. *Journal of Climate*, 19(19):4755–4771.

Power, S. B. and Smith, I. N. (2007). Weakening of the walker circulation and apparent dominance of el niño both reach record levels, but has enso really changed? *Geophysical Research Letters*, 34(18).

Raddatz, T., Reick, C., Knorr, W., Kattge, J., Roeckner, E., Schnur, R., Schnitzler, K.-G., Wetzel, P., and Jungclaus, J. (2007). Will the tropical land biosphere dominate the climate–carbon cycle feedback during the twenty-first century? *Climate dynamics*, 29(6):565–574.

Rasmusson, E. M. and Carpenter, T. H. (1982). Variations in tropical sea surface temperature and surface wind fields associated with the southern oscillation/el niño. *Monthly Weather Review*, 110(5):354–384.

Rein, B., Lückge, A., Reinhardt, L., Sirocko, F., Wolf, A., and Dullo, W.-C. (2005). El niño variability off peru during the last 20,000 years. *Paleoceanography*, 20(4).

Renoult, M., Annan, J. D., Hargreaves, J. C., Sagoo, N., Flynn, C., Kapsch, M.-L., Li, Q., Lohmann, G., Mikolajewicz, U., Ohgaito, R., et al. (2020). A bayesian framework for emergent constraints: case studies of climate sensitivity with pmip. *Climate of the Past*, 16(5):1715–1735.

Shi, X. and Lohmann, G. (2016). Simulated response of the mid-holocene atlantic meridional overturning circulation in echam6-fesom/mpiom. *Journal of Geophysical Research: Oceans*, 121(8):6444–6469.

Shi, X., Lohmann, G., Sidorenko, D., and Yang, H. (2020). Early-holocene simulations using different forcings and resolutions in awi-esm. *The Holocene*, page 0959683620908634.

Sidorenko, D., Goessling, H., Koldunov, N., Scholz, P., Danilov, S., Barbi, D., Cabos, W., Gurses, O., Harig, S., Hinrichs, C., et al. (2019). Evaluation of fesom2. 0 coupled to echam6. 3: Preindustrial and highresmip simulations. *Journal of Advances in Modeling Earth Systems*, 11(11):3794–3815.

Sidorenko, D., Wang, Q., Danilov, S., and Schröter, J. (2011). Fesom under coordinated ocean-ice reference experiment forcing. *Ocean Dynamics*, 61(7):881–890.

Stein, K., Timmermann, A., Schneider, N., Jin, F.-F., and Stuecker, M. F. (2014). Enso seasonal synchronization theory. *Journal of Climate*, 27(14):5285–5310.

Stevens, B., Giorgetta, M., Esch, M., Mauritsen, T., Crueger, T., Rast, S., Salzmann, M., Schmidt, H., Bader, J., Block, K., et al. (2013). Atmospheric component of the mpi-m earth system model: Echam6. *Journal of Advances in Modeling Earth Systems*, 5(2):146–172.

Sundqvist, H., Berge, E., and Kristjánsson, J. E. (1989). Condensation and cloud parameterization studies with a mesoscale numerical weather prediction model. *Monthly Weather Review*, 117(8):1641–1657.

Timm, O., Timmermann, A., Abe-Ouchi, A., Saito, F., and Segawa, T. (2008). On the definition of seasons in paleoclimate simulations with orbital forcing. *Paleoceanography*, 23(2).

Timmermann, R., Danilov, S., Schröter, J., Böning, C., Sidorenko, D., and Rollenhagen, K. (2009). Ocean circulation and sea ice distribution in a finite element global sea ice–ocean model. *Ocean modelling*, 27(3-4):114–129.

Toniazzo, T., Collins, M., and Brown, J. (2008). The variation of enso characteristics associated with atmospheric parameter perturbations in a coupled model. *Climate dynamics*, 30(6):643–656.

Torrence, C. and Webster, P. J. (1998). The annual cycle of persistence in the el nño/southern oscillation. *Quarterly Journal of the Royal Meteorological Society*, 124(550):1985–2004.

Torrence, C. and Webster, P. J. (1999). Interdecadal changes in the enso–monsoon system. *Journal of climate*, 12(8):2679–2690.

Trenberth, K. E. (1997). The definition of el nino. *Bulletin of the American Meteorological Society*, 78(12):2771–2778.

Trenberth, K. E. and Caron, J. M. (2000). The southern oscillation revisited: Sea level pressures, surface temperatures, and precipitation. *Journal of Climate*, 13(24):4358–4365.

Trenberth, K. E. and Stepaniak, D. P. (2001). Indices of el niño evolution. *Journal of climate*, 14(8):1697–1701.

Troup, A. (1965). The 'southern oscillation'. *Quarterly Journal of the Royal Meteorological Society*, 91(390):490–506.

Tudhope, A. W., Chilcott, C. P., McCulloch, M. T., Cook, E. R., Chappell, J., Ellam, R. M., Lea, D. W., Lough, J. M., and Shimmield, G. B. (2001). Variability in the el niño-southern oscillation through a glacial-interglacial cycle. *Science*, 291(5508):1511–1517.

Valcke, S. (2013). The oasis3 coupler: A european climate modelling community software. *Geoscientific Model Development*, 6(2):373.

Van Oldenborgh, G. J. and Burgers, G. (2005). Searching for decadal variations in enso precipitation teleconnections. *Geophysical Research Letters*, 32(15).

Vorrath, M.-E., Müller, J., Rebolledo, L., Cárdenas, P., Shi, X., Esper, O., Opel, T., Geibert, W., Muñoz, P., Haas, C., et al. (2020). Sea ice dynamics in the bransfield strait, antarctic peninsula, during the past 240 years: a multi-proxy intercomparison study. *Climate of the Past*, 16(6):2459–2483.

Wang, B. (1995). Interdecadal changes in el nino onset in the last four decades. *Journal of Climate*, 8(2):267–285.

Wang, Q., Danilov, S., Sidorenko, D., Timmermann, R., Wekerle, C., Wang, X., Jung, T., and Schröter, J. (2013). The finite element sea ice-ocean model (fesom): formulation of an unstructured-mesh ocean general circulation model. *Geosci. Model Dev. Discuss*, 6(3):3893–3976.

Yeh, S.-W. and Kirtman, B. P. (2005). Pacific decadal variability and decadal enso amplitude modulation. *Geophysical Research Letters*, 32(5).

Zhang, R.-H., Busalacchi, A. J., and DeWitt, D. G. (2008). The roles of atmospheric stochastic forcing (sf) and oceanic entrainment temperature (te) in decadal modulation of enso. *Journal of climate*, 21(4):674–704.